ℭ

Resonating valence bond states in the PEPS formalism

Norbert Schuch,[1,2] Didier Poilblanc,[3] J. Ignacio Cirac,[4] and David Pérez-García[5]

[1]*Institut für Quanteninformation, RWTH Aachen, 52056 Aachen, Germany*
[2]*Institute for Quantum Information, California Institute of Technology, MC 305-16, Pasadena, California 91125, USA*
[3]*Laboratoire de Physique Théorique, CNRS and Université de Toulouse, 31062 Toulouse, France*
[4]*Max-Planck-Institut für Quantenoptik, Hans-Kopfermann-Straße 1, D-85748 Garching, Germany*
[5]*Departamento Analisis Matematico and IMI, Universidad Complutense de Madrid, E-28040 Madrid, Spain*

We study resonating valence bond (RVB) states in the projected entangled pair states (PEPS) formalism. Based on symmetries in the PEPS description, we establish relations between the toric code state, the orthogonal dimer state, and the SU(2) singlet RVB state on the kagome lattice: We prove the equivalence of toric code and dimer state, and devise an interpolation between the dimer state and the RVB state. This interpolation corresponds to a continuous path in Hamiltonian space, proving that the RVB state is the fourfold degenerate ground state of a local Hamiltonian on the (finite) kagome lattice. We investigate this interpolation using numerical PEPS methods, studying the decay of correlation functions, the change of overlap, and the entanglement spectrum, none of which exhibits signs of a phase transition.

I. INTRODUCTION

Resonating valence bond (RVB) states have been introduced by Anderson[1] as a wave function in the context of high-temperature superconductivity and have since then received significant attention. RVB wave functions are obtained as the superposition of all nearest-neighbor (or otherwise constrained) singlet coverings on a given lattice, and they have been studied as an ansatz capturing the behavior of frustrated quantum spin systems, in particular Heisenberg antiferromagnets on frustrated lattices.[2] They are believed to describe so-called *topological spin liquids*, i.e., exotic phases with degenerate ground states which however do not break rotational or translational symmetry, despite the presence of strong antiferromagnetic interactions. Particular interest, both theoretically and experimentally, has been devoted to frustrated magnets on the kagome lattice, as those systems are realized in actual materials and form candidates for the first experimental observation of a topological spin liquid.[3–7]

Unfortunately, models with potential RVB ground states are typically difficult to study. One the one hand, this is due to presence of frustration. Yet, the bigger issue seems to be that different singlet configurations are not orthogonal, which up to now has, e.g., hindered a full understanding of how RVB states appear as ground states of local Hamiltonians.[8] In order to better understand the RVB phase, simplified so-called *dimer models* have been introduced,[9] where the system is redefined on the Hilbert space spanned by all dimer coverings of the lattice, making different dimer configurations orthogonal by definition. Dimer models have subsequently been studied for various lattices, and it has in particular been found that for certain geometries, such as for the triangular[10] or the kagome lattice,[11] such states appear as ground states of local Hamiltonians with topological ground state degeneracy (fourfold on the torus), forming a $\mathbb{Z}_2$ topological spin liquid. Unfortunately, these findings cannot be mapped back to the true RVB state due to the different underlying Hilbert spaces which are not related by a simple mapping, and thus, the way in which the corresponding RVB states can describe ground states

of local Hamiltonians is only partially understood (although very remarkable progress in this direction has been made during the last years[8,12]).

More recently, projected entangled pair states (PEPS) have been introduced as a tool to study quantum many-body wave functions.[13,14] PEPS give a description of quantum many-body states based on their entanglement structure in terms of local tensors, and form a framework which allows us to both analytically understand these wave functions and to study their properties numerically. In particular, there is a clear way to understand how PEPS arise as ground states of local Hamiltonians, especially for systems with unique ground states[15] and with topological order,[16] based on the symmetry properties of the underlying tensor representation. Numerically, they form a tool for computing quantities such as correlation functions or overlaps efficiently with very high accuracy, using transfer operators of matrix product form.[14]

In this paper, we perform a systematic study of RVB and dimer states in the PEPS formalism, focusing on the kagome lattice. We introduce closely related PEPS representations for the RVB wave function[17] and a version of the dimer state in which different dimer configurations are locally orthogonal. These representations allow us to derive a reversible local mapping between the RVB and the dimer state, as well as to prove local unitary equivalence of the dimer state and Kitaev's toric code.[18] This yields a Hamiltonian for our dimer model, and subsequently a Hamiltonian for the RVB state: That is, we can for the first time prove that the RVB state on the kagome lattice is the ground state of a local Hamiltonian with topological ground state degeneracy (fourfold on the torus) for any finite lattice. The PEPS formalism further allows us to construct an interpolation between RVB and dimer state where the Hamiltonian changes smoothly along the path. Using techniques for numerical PEPS calculations,[14] we try to assess whether the RVB state is in the same phase as the dimer state (which is equivalent to the toric code and thus a $\mathbb{Z}_2$ topological spin liquid) by looking for signatures of a phase transition along the dimer-RVB interpolation. We have

considered the behavior of correlation functions, the rate at which the ground state changes in terms of the wave function overlap,[19] and the entanglement spectrum of the system, and have found that all of these quantities behave smoothly and show no sign of a phase transition.

Let us describe the organization of the paper. For the sake of conciseness, alternative definitions, proofs, etc., have been moved to appendices. In Sec. II, we introduce the RVB and dimer states and their PEPS representations, as well as the formulation using tensor networks. Alternative PEPS representations are discussed in Appendix A. In Sec. III, we discuss the relations between the toric code, the dimer state, and the RVB state, using the symmetry of the underlying tensors. Based on these findings, we show how to construct a smooth interpolation between the dimer state and the RVB state in Sec. IV, and subsequently study its properties numerically. In Sec. V, we use the relation between the toric code, the dimer state, and the RVB state to construct parent Hamiltonians for the dimer state and the RVB, as well as a smooth path of Hamiltonians for the interpolation between them. Appendix C provides a simpler parent Hamiltonian for the dimer state, based on a more direct mapping to the toric code, and Appendix D shows how to directly derive a (much more compact) parent Hamiltonian for the RVB state by generalizing the techniques developed in Ref. 16 for PEPS with symmetries to the symmetries found in the RVB.

II. DEFINITIONS

A. The RVB and orthogonal RVB state

We start by introducing dimer states and resonating valence bond (RVB) states. We focus on the kagome lattice, Fig. 1(a), both for its relevance and for clarity of the presentation; but our techniques generalize to other lattices (see conclusions). A *dimer* is a pair of vertices connected by an edge. A *dimer covering* is a complete covering of the lattice with dimers, Fig. 1(b). We can associate orthogonal quantum states $|D\rangle$ with each dimer covering D. Then, the *dimer state* is given by the equal weight superposition $|\Psi_{\text{dimer}}\rangle = \sum |D\rangle$, where the sum runs over all dimer coverings D. Usually, it is favorable to ensure orthogonality of different states $|D\rangle$ and $|D'\rangle$ locally; we will introduce such a version of the dimer state which is particularly suited for our purposes in Sec. II C.

Let us now turn towards the resonating valence bond (RVB) state. We first associate with each vertex of the lattice a spin-$\frac{1}{2}$ particle, or qubit, with basis states $|0\rangle \equiv |\uparrow\rangle$ and $|1\rangle \equiv |\downarrow\rangle$. Then, for each dimer covering D we define a state $|\sigma(D)\rangle$ which is a tensor product of singlets $|01\rangle - |10\rangle$ (we omit normalization throughout) between the pairs of spins in each dimer in the covering, where the singlets are oriented according to the arrows in Fig. 1(a). The *resonating valence bond* (RVB) state is then defined as the equal weight superposition $|\Psi_{\text{RVB}}\rangle = \sum_D |\sigma(D)\rangle$ over all dimer coverings.

B. PEPS representation of the RVB state

We will now give a description of the RVB state in terms of projected entangled pair states (PEPS).[13] PEPS are states which can be described by first placing "virtual" entangled states between the sites of the system, and subsequently applying linear maps at each site to obtain the physical system. A PEPS representation of RVB states has first been given in Ref. 17; a detailed discussion how it is related to our description can be found in Appendix A.

To obtain a PEPS description of the RVB state, we first place 3-qutrit states

$$|\varepsilon\rangle = \sum_{i,j,k=0}^{2} \varepsilon_{ijk}|ijk\rangle + |222\rangle \tag{1}$$

inside each triangle of the kagome lattice, as depicted in Fig. 2. Here, ε_{ijk} is the completely antisymmetric tensor with $\varepsilon_{012} = 1$, and i, j, and k are oriented clockwise [i.e., consistent with the arrows in Fig. 1(a)]. Second, we apply the map

$$\mathcal{P} = |0\rangle(\langle 02| + \langle 20|) + |1\rangle(\langle 12| + \langle 21|) \tag{2}$$

at each vertex, which maps the two qutrits from the adjacent $|\varepsilon\rangle$ states to one qubit. It is straightforward to check that this construction exactly gives the resonating valence bond state defined above (see Appendix A for a detailed discussion).

C. PEPS representation of dimer state

In a similar way as for the RVB state, we can also obtain a PEPS representation of the dimer state. To this end, we enlarge our local Hilbert space and replace the map $\mathcal{P}$ in Fig. 2 by the map

$$\mathcal{P}_{\perp} = |02\rangle\langle 02| + |12\rangle\langle 12| + |20\rangle\langle 20| + |21\rangle\langle 21|. \tag{3}$$
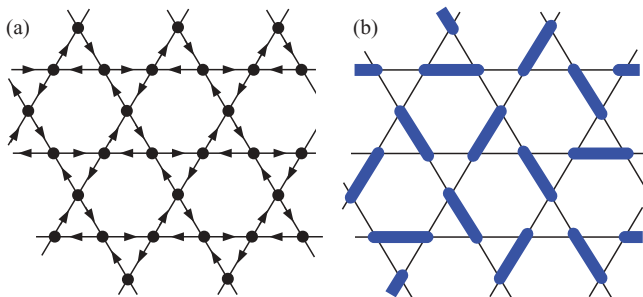

FIG. 1. (Color online) (a) Oriented kagome lattice. Spins are associated with vertices. (b) Dimer covering of the kagome lattice. The lattice is completely covered with *dimers* (marked blue), i.e., disjoint pairs of adjacent vertices.
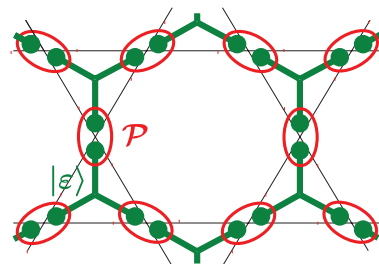

FIG. 2. (Color online) PEPS construction of the RVB state: Place $|\epsilon\rangle$ states (green), Eq. (1), and then apply the map $\mathcal{P}$ (red), Eq. (2), as indicated. To obtain the dimer state, replace $\mathcal{P}$ with $\mathcal{P}_{\perp}$, Eq. (3).

It is straightforward to check that the resulting state is an equal weight superposition of all dimer coverings, and that different dimer configurations are orthogonal, since the position of the dimers can be unambiguously inferred from the location of the $|2\rangle$'s. Note that while we write the physical space as a subspace of a 3×3-dimensional space, in fact only a four-dimensional subspace is used. A more detailed discussion of the construction can again be found in Appendix A.

As one might expect, it is possible to obtain the RVB state from the dimer state by coherently discarding the information about where the singlet is located and only keeping the singlet subspace span$\{|0\rangle,|1\rangle\}$. This is most easily seen by noting that

$$\mathcal{P} = \mathcal{P}\mathcal{P}_\perp,$$

and thus applying $\mathcal{P}$ to each site of the dimer state yields the RVB state.

Note that our representation of the dimer state differs from the formulations typically used in the literature in two points: First, while dimer models have been usually studied on the space spanned by valid dimer configurations, our formulation allows to locally check whether a dimer is present on a given link. This allows us to enforce the restriction to the space of valid dimer configurations using a local Hamiltonian, and ultimately enables us to map our dimer model to the toric code by local unitaries. Second, unlike mappings where the presence or absence of a dimer is represented by a spin,[20] our mapping uses actual singlets built of two entangled particles. This allows us to locally interpolate between the dimer and the RVB model, and gives rise to a gapped entanglement spectrum, which is in contrast to the gapless entanglement spectra which had been observed previously for topologically ordered systems.

D. Gauge transformation

The PEPS representation of the RVB and dimer state are built using unnormalized singlets, as the weight of $|01\rangle - |10\rangle$ and $|22\rangle$ in Eq. (1) is the same. Since the number of singlets in all dimer configurations is the same, this is not an issue; however, in some situations (cf. Sec. III B) it will be more convenient to normalize the singlets, i.e., replace (1) by

$$|\hat{\varepsilon}\rangle = \frac{1}{\sqrt{2}} \sum_{i,j,k=0}^{2} \varepsilon_{ijk}|ijk\rangle + |222\rangle. \tag{4}$$

Note that $|\hat{\varepsilon}\rangle = (Y \otimes Y \otimes Y)|\varepsilon\rangle$, where $Y = \mathrm{diag}(2^{-1/4}, 2^{-1/4}, 1)$. Since on the other hand, $\mathcal{P}_\perp(Y \otimes Y) = 2^{-1/4}\mathcal{P}_\perp$ (and thus also for $\mathcal{P}$, as well as the interpolation defined in Sec. IV), we find that these two PEPS do not only represent the same total state, but are in fact related by a *local* gauge transformation, allowing us to directly relate all properties of their PEPS description.

E. The toric code

Consider a square lattice of qubits, with an A-B pattern on the plaquettes, Fig. 3(a). Kitaev's toric code state[18] is the ground state of the Hamiltonian

$$H_{\mathrm{TC}} = \sum_{p_A} \frac{1}{2}\big(1 - Z_{p_A}^{\otimes 4}\big) + \sum_{p_B} \frac{1}{2}\big(1 - X_{p_B}^{\otimes 4}\big), \tag{5}$$
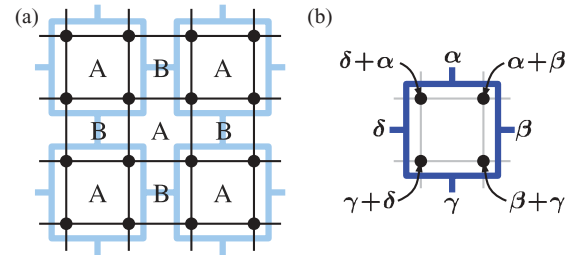

FIG. 3. (Color online) Construction of the toric code as a tensor network. (a) The toric code is defined on a square lattice with two types of plaquettes. By taking 2×2 blocks over A-type plaquettes, a particularly convenient tensor network description can be found. (b) Tensor for the toric code; depicted are the nonzero entries. The four auxiliary indices are in the X basis, while the physical sites are in the Z basis.

where the sums run over all A and B type plaquettes p_A and p_B, respectively, and the tensor products of Paulis act on the qubits adjacent to each plaquette.

The toric code state can be written as a PEPS[17] with bond dimension $D = 2$. A particularly useful representation is obtained by blocking the qubits in 2×2 blocks around A-type plaquettes, as indicated in Fig. 3(a) and letting the PEPS projector be[16]

$$\mathcal{P}_{\mathrm{TC}} = \sum_{\alpha,\beta,\gamma,\delta=0}^{1} |\alpha+\beta,\beta+\gamma,\gamma+\delta,\delta+\alpha\rangle\langle\hat{\alpha},\hat{\beta},\hat{\gamma},\hat{\delta}| \tag{6}$$

for each of these blocks. Here, the sums are modulo 2, and the ordering of the indices is illustrated in Fig. 3(b); the virtual qubits are expressed in the X eigenbasis $|\hat{0}\rangle = (|0\rangle + |1\rangle)/\sqrt{2}$, $|\hat{1}\rangle = (|0\rangle - |1\rangle)\sqrt{2}$.

F. Formulation using tensor networks

PEPS can also be expressed in terms of *tensor networks*; while both descriptions are mathematically equivalent we will utilize either of them when more convenient.

A tensor network state is a state

$$|\psi\rangle = \sum_{i_1,\ldots,i_N=0}^{1} c_{i_1 \ldots i_N}|i_1,\ldots,i_N\rangle, \tag{7}$$

where $c_{i_1 \ldots i_N}$ can be expressed efficiently by a tensor network, i.e., as the sum over $\alpha_1,\ldots,\alpha_M$ of product of tensors with indices $i_1,\ldots,i_N$ and $\alpha_1,\ldots,\alpha_M$, where each of the tensors only has a few indices. Tensor networks are often expressed graphically, with tensors denoted by boxes with legs corresponding to the indices, where connecting legs corresponds to contracting over the corresponding index; cf. Fig. 4(a).

It is straightforward to see that the simplified PEPS representation of the RVB state can be expressed using two types tensors, E and P, defined such that

$$|\varepsilon\rangle \equiv \sum_{\alpha\beta\gamma} E^{\alpha\beta\gamma}|\alpha,\beta,\gamma\rangle \tag{8}$$
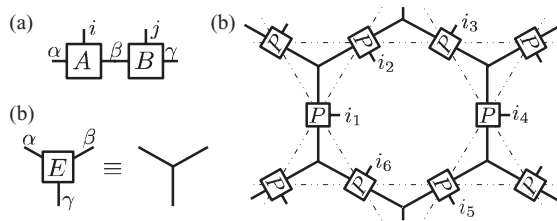
FIG. 4. Tensor network notation for the RVB state. (a) Tensors are denoted as boxes with one leg per index. Connecting legs correspond to summing over that index; this panel, e.g., shows $\sum_\beta A^i_{\alpha\beta} B^j_{\beta\gamma}$. (b) Tensor network description of the RVB state; the triangular link is shorthand for the tensor E implicitly defined in Eq. (8); see panel (c). Depending on whether we choose P as in Eq. (9) or replace it with $P_\perp$, Eq. (10), we obtain a tensor network for either the RVB or the dimer state; in the latter case, the physical indices i_k form double indices (i_k, j_k).

and

$$\mathcal{P} \equiv \sum_{i\eta\vartheta} P^i_{\eta\vartheta} |i\rangle\langle \eta,\vartheta|, \tag{9}$$

which form the tensor network of Fig. 4(b) [where we use the shorthand Fig. 4(c) for E]; it has open indices $i_1, \ldots, i_N$ and yields the coefficient $c_{i_1,\ldots,i_N}$ in Eq. (7). Again, we can replace P by $P_\perp$ defined by

$$\mathcal{P}_\perp \equiv \sum_{ij\eta\vartheta} (P_\perp)^{ij}_{\eta\vartheta} |i,j\rangle\langle \eta,\vartheta| \tag{10}$$

to obtain a PEPS representation of the dimer state.

III. RELATIONS

In this section, we will show how one can transform reversibly between the toric code, the dimer state, and the RVB state. To this end, we will start by recalling the concept of G injectivity of PEPS[16] and subsequently apply it it to prove equivalence of the toric code and the dimer state, and to devise a mapping which transforms between the dimer and the RVB state.

A. $\mathbb{Z}_2$ injectivity

We start by introducing $\mathbb{Z}_2$ *injectivity*, which has been introduced (as G injectivity, with G any finite group) in Ref. 16 as a tool to characterize PEPS with topological properties. Let $\bar{Z}$ be a unitary such that $\{\mathbb{1}, \bar{Z}\}$ forms a representation of $\mathbb{Z}_2$; i.e., $\bar{Z}^2 = \mathbb{1}$. A $\mathbb{Z}_2$-*invariant* tensor network consists of tensors which are invariant under the symmetry action on all virtual indices simultaneously, as depicted in Fig. 5(a) (we restrict to equal representations on all indices). This property is stable under blocking; i.e., two (or more) $\mathbb{Z}_2$-invariant tensors together are still $\mathbb{Z}_2$ invariant; see Fig. 5(b). A $\mathbb{Z}_2$-invariant tensor is called $\mathbb{Z}_2$ *injective* if the corresponding PEPS projector $\mathcal{P}$ is injective on the invariant subspace (the subspace belonging to the trivial representation), i.e., if it has a left inverse $\mathcal{P}^{-1}$ such that $\mathcal{P}^{-1}\mathcal{P}$ is the projection onto the invariant subspace. Differently speaking, this means that there exists a linear map which we can apply to the physical system to obtain direct access to the virtual system, up to a projection onto the symmetric subspace Π_S. $\mathbb{Z}_2$ injectivity is stable under
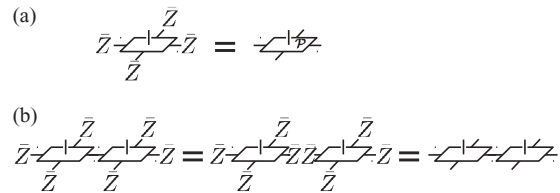

FIG. 5. $\mathbb{Z}_2$-invariant tensor network. (a) A tensor is called $\mathbb{Z}_2$ invariant if it is invariant under some $\bar{Z}$ applied to all virtual indices, where $\{1, \bar{Z}\}$ forms a representation of $\mathbb{Z}_2$. (b) $\mathbb{Z}_2$ invariance is stable under concatenation of tensors.

concatenation: When composing two $\mathbb{Z}_2$-injective tensors, we obtain another $\mathbb{Z}_2$-injective tensor.[16]

The key point to note is that any two $\mathbb{Z}_2$-injective tensor networks with identical geometry and symmetry representation, but different tensors, are locally equivalent: There exists a map acting on the physical system of individual tensors which transforms the networks into another. This follows since both PEPS projectors, $\mathcal{P}_A$ and $\mathcal{P}_B$, have left inverses which yield the projector Π_S onto the symmetric subspace, $\mathcal{P}_A^{-1}\mathcal{P}_A = \mathcal{P}_B^{-1}\mathcal{P}_B = \Pi_S$, and thus $\mathcal{P}_A = (\mathcal{P}_A\mathcal{P}_B^{-1})\mathcal{P}_B$, and vice versa.

An important special case are $\mathbb{Z}_2$-*isometric* tensors where $\mathcal{P}$ is a partial isometry, $\mathcal{P}^{-1} = \mathcal{P}^\dagger$: Any two $\mathbb{Z}_2$-isometric tensors $\mathcal{P}_A$ and $\mathcal{P}_B$ can be transformed into each other by a unitary acting on the physical system. Again, $\mathbb{Z}_2$ isometry is a property which is stable under concatenation.[16]

B. Toric code and dimer state

In the following, we will show that the toric code state and the orthogonal dimer state are both built of $\mathbb{Z}_2$-isometric tensors, which implies that they can be transformed into each other by local unitaries. (This relation has been observed previously by mapping the presence or absence of dimers to a spin degree of freedom.[20]) In this section, we will consider the $\mathbb{Z}_2$ representation $\{\mathbb{1}, Z\}$, with $Z = \left(\begin{smallmatrix} 1 & \\ & -1 \end{smallmatrix}\right)$.

For the toric code tensor Eq. (6), it is straightforward to check that it is invariant under $Z^{\otimes 4}$ and acts isometrically on the invariant subspace, i.e., is $\mathbb{Z}_2$ isometric. In order to see the same for the dimer state, we first rewrite $P_\perp$, Eq. (10), as

$$P_\perp = \sum_{k=0}^{1} A_k \otimes B_k, \tag{11}$$

where $A_0 = B_1 = |0\rangle\langle 0| + |1\rangle\langle 1|$, and $A_1 = B_0 = |2\rangle\langle 2|$. Using this decomposition, we replace each tensor $P_\perp$ in Fig. 4(b) with a pair of tensors A and B connected by a two-dimensional bond, cf. Fig. 6(a), oriented as in Fig. 6(b). This orientation allows us to block the tensors into triangles, labeled A and B, containing only A and B type tensors, cf. Fig. 6(b); the triangles are connected by bonds of dimension two.

The bonds are associated with vertices; a bond state $|0\rangle$ ($|1\rangle$) indicates that the dimer lies inside the A (B) triangle (similar to the "arrow representation" of Ref. 21). As each triangle contains either no or one dimer, the A (B) tensors are odd (even) under $Z^{\otimes 3}$ symmetry, and moreover isometric on the (anti)symmetric subspace if we use the gauge of Eq. (4); the possible mappings from bond to physical configurations are given in Fig. 7.
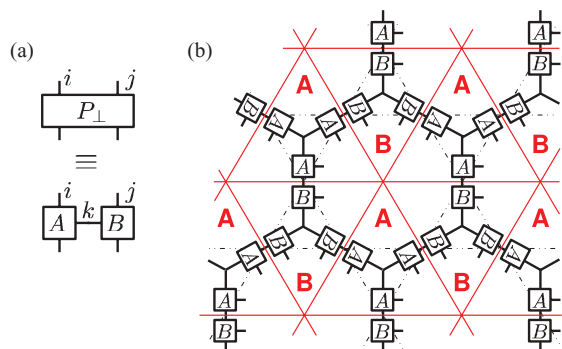
FIG. 6. (Color online) Transformation of the dimer state into the toric code. (a) $P_\perp$ can be rewritten as a tensor network with bond dimension 2. (b) Network obtained by replacing $P_\perp$ in Fig. 4(b) with the tensor network of panel (a). The tensor network can be grouped into triangular tensors which contain only A or B tensors, and which are connected by bonds of dimension 2.

We now group one A and one B tensor to obtain square tensors, which are antisymmetric and isometric; grouping two of these square tensors finally yields a $\mathbb{Z}_2$-isometric tensor with symmetry representations Z and $Z \otimes Z$, respectively. Blocking two tensors of the toric code also yields a $\mathbb{Z}_2$-isometric tensor with the very same symmetry, and thus the dimer state and the toric code can be converted into one another by local unitaries.

C. RVB and dimer state

Let us now show that we can reversibly (though not unitarily) transform the dimer state to the RVB state. In principle, the forward direction is obvious, as $\mathcal{P} = \mathcal{P}\mathcal{P}_\perp$; however, this transformation cannot be inverted. In order to construct an invertible transformation, we will show that both states can be understood as being constructed from $\mathbb{Z}_2$-injective tensors connected by $|\varepsilon\rangle$ bonds: Following the reasoning of Sec. III A, we can reversibly transform between the two $\mathbb{Z}_2$-injective tensors and thus between the RVB state and the dimer state.

For this section, we will use the PEPS representation Fig. 4 of both the RVB and the dimer state. The representation of the
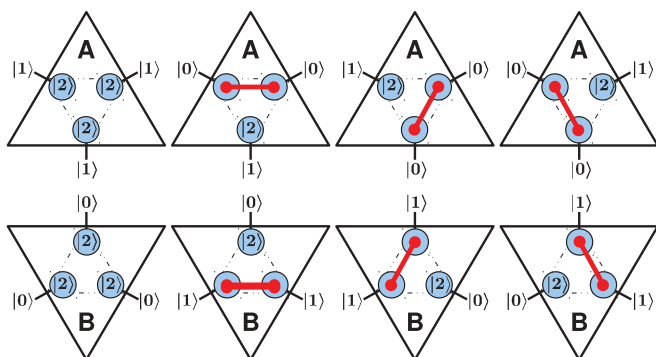

FIG. 7. (Color online) Nonzero orthogonal virtual states and the corresponding orthogonal physical states for the dimer state tensors (the red lines denotes singlets). The A (B) type tensors are supported on the odd (even) parity subspace.
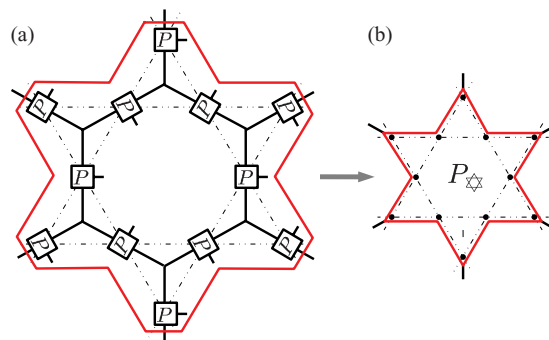

FIG. 8. (Color online) Definition of the tensor $P_{\bigstar}$. (a) $P_{\bigstar}$ is obtained by blocking 12 tensors P with 6 triangular "bond tensors" E; it maps 6 virtual qutrits to 12 physical qubits. (b) Effective depiction of the tensor $P_{\bigstar}$.

$\mathbb{Z}_2$ symmetry is given by

$$\bar{Z} := \begin{pmatrix} 1 & & \\ & 1 & \\ & & -1 \end{pmatrix}.$$

It is straightforward to see that both P, $P_\perp$, and the bond tensor E are antisymmetric under the action of the symmetry on all virtual indices. Let us now form a new tensor by blocking all the tensors covering one star; cf. Fig. 8. We call the new tensors $P_{\bigstar}$ and $P_{\perp,\bigstar}$, respectively (with corresponding PEPS projector $\mathcal{P}_{\bigstar}$ and $\mathcal{P}_{\perp,\bigstar}$). Clearly, we can tile the lattice with $P_{\bigstar}$ tensors connected by E bonds; see Fig. 9. Due to stability of $\mathbb{Z}_2$ invariance, one finds that $P_{\bigstar}$ and $P_{\perp,\bigstar}$ are $\mathbb{Z}_2$ invariant. On the other hand, it can be checked analytically using a computer algebra system that $\mathcal{P}_{\bigstar}$ is indeed invertible on the invariant subspace of $\bar{Z}^{\otimes 6}$; i.e., $\mathcal{P}_{\bigstar}$ is $\mathbb{Z}_2$ injective. This immediately implies $\mathbb{Z}_2$ injectivity of $P_{\perp,\bigstar}$ (as $\mathcal{P}_{\bigstar} = \mathcal{P}^{\otimes 6}\mathcal{P}_{\perp,\bigstar}$).
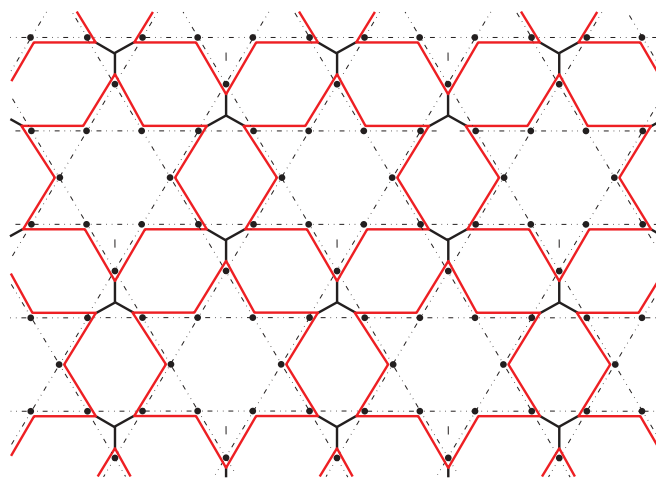

FIG. 9. (Color online) Complete covering of the kagome lattice with stars, Fig. 8. The stars tensor $P_{\bigstar}$ (or projectors $\mathcal{P}_{\bigstar}$), together with triangular tensors E (or $|\varepsilon\rangle$ bonds), describe the RVB state (or its orthogonal version, if we choose $P_{\perp,\bigstar}$ instead). By acting with $\mathcal{O}_{\bigstar}$ on each of the stars, we can reversibly convert between the RVB and the orthogonal RVB.

We can now use the argument of Sec. III A to construct an invertible mapping: $\mathbb{Z}_2$ injectivity of $\mathcal{P}_{\stackrel{.}{\cancel\star}}$ implies the existence of $\mathcal{P}_{\stackrel{.}{\cancel\star}}^{-1}$ such that $\mathcal{P}_{\stackrel{.}{\cancel\star}}^{-1}\mathcal{P}_{\stackrel{.}{\cancel\star}}$ is the projector onto the $\bar{Z}^{\otimes 6}$-invariant subspace on the virtual qutrits along the boundary of the star. If we now define $\mathcal{O}_{\stackrel{.}{\cancel\star}} = \mathcal{P}_{\perp,\stackrel{.}{\cancel\star}}\mathcal{P}_{\stackrel{.}{\cancel\star}}^{-1}$, it follows that $\mathcal{O}_{\stackrel{.}{\cancel\star}}\mathcal{P}_{\stackrel{.}{\cancel\star}} = \mathcal{P}_{\perp,\stackrel{.}{\cancel\star}}$; i.e., it (locally) converts the RVB into the dimer state. [Note that $\mathcal{O}_{\stackrel{.}{\cancel\star}}$ is only well defined on the range of $\mathcal{P}_{\stackrel{.}{\cancel\star}}$, rg($\mathcal{P}_{\stackrel{.}{\cancel\star}}$); we choose $\mathcal{O}_{\stackrel{.}{\cancel\star}}$ to vanish on its orthogonal complement.] Analogously, we can define $\mathcal{O}_{\stackrel{.}{\cancel\star}}^{-1}$ such that $\mathcal{O}_{\stackrel{.}{\cancel\star}}^{-1}\mathcal{P}_{\perp,\stackrel{.}{\cancel\star}} = \mathcal{P}_{\stackrel{.}{\cancel\star}}$ [again such that it vanishes on rg($\mathcal{P}_{\perp,\stackrel{.}{\cancel\star}}$)$^\perp$], and it is easily verified that $\mathcal{O}_{\stackrel{.}{\cancel\star}}^{-1}\mathcal{O}_{\stackrel{.}{\cancel\star}} = \mathbb{1}_{\mathrm{rg}(\mathcal{P}_{\stackrel{.}{\cancel\star}})}$ and $\mathcal{O}_{\stackrel{.}{\cancel\star}}\mathcal{O}_{\stackrel{.}{\cancel\star}}^{-1} = \mathbb{1}_{\mathrm{rg}(\mathcal{P}_{\perp,\stackrel{.}{\cancel\star}})}$; i.e., $O_{\stackrel{.}{\cancel\star}}^{-1}$ is the pseudoinverse of $O_{\stackrel{.}{\cancel\star}}$.

Applying the maps $\mathcal{O}_{\stackrel{.}{\cancel\star}}$ or its inverse to all $K = N/12$ stars in the tiling Fig. 9, we can now reversibly convert between the dimer and the RVB state, $|\Psi_{\mathrm{dimer}}\rangle = \mathcal{O}_{\stackrel{.}{\cancel\star}}^{\otimes K}|\Psi_{\mathrm{RVB}}\rangle$ and $|\Psi_{\mathrm{RVB}}\rangle = (O_{\stackrel{.}{\cancel\star}}^{-1})^{\otimes K}|\Psi_{\mathrm{oRVB}}\rangle$.

IV. INTERPOLATION

A. Interpolation between dimer model and RVB

Let us now show how to continuously deform the dimer state into the RVB state; as we will show in Sec. V C, this interpolation does correspond to a continuous change of the associated local parent Hamiltonian. To this end, we define a family of PEPS projectors

$$\mathcal{P}(\theta) = |+\rangle[|0\rangle(\langle 02| + \langle 20|) + |1\rangle(\langle 12| + \langle 21|)]$$
$$+ \theta|-\rangle[|0\rangle(\langle 02| - \langle 20|) + |1\rangle(\langle 12| - \langle 21|)] \quad (12)$$

with a two-qubit physical space. Clearly, $\mathcal{P}(0) \equiv \mathcal{P}$ and $\mathcal{P}(1) \equiv \mathcal{P}_\perp$, both up to local isometries. By placing $\mathcal{P}(\theta)$ in the tensor network Fig. 2, we therefore obtain a smooth interpolation $|\Psi(\theta)\rangle$ between the RVB and the dimer state. Clearly, we can accordingly define $P_{\stackrel{.}{\cancel\star}}(\theta)$ and subsequently $\mathcal{O}_{\stackrel{.}{\cancel\star}}(\theta) = \mathcal{P}_{\stackrel{.}{\cancel\star}}(\theta)\mathcal{P}_{\stackrel{.}{\cancel\star}}^{-1}$, which is a continuous invertible map from rg $\mathcal{P}_{\stackrel{.}{\cancel\star}}$ to rg $\mathcal{P}_{\stackrel{.}{\cancel\star}}(\theta)$. Note that while it might seem that the interpolation (12) results in a discontinuity as $\theta \to 0$, the discussion about the equivalence of RVB and dimer state in the preceding section shows that this discontinuity disappears when considering whole stars.

This interpolation can be understood as a way to make different dimer configurations more and more orthogonal, analogous to what is achieved by decorating the lattice in Ref. 22: Overlapping two different dimer configurations gives rise to a loop pattern, and the absolute value of their overlap is x^{L-2N}, with N the number of loops (including length-2 ones) and L their total length (which equals the number of lattice sites). Here, $x = 1/\sqrt{2}$ for the RVB and $x = 0$ for the dimer state, and Eq. (12) corresponds to an interpolation $x(\theta) = \frac{1}{\sqrt{2}}\frac{1-\theta^2}{1+\theta^2}$.

B. Numerical results

We have numerically studied the interpolation (12) between the dimer state (which is a topological $\mathbb{Z}_2$ spin liquid) and the RVB state to determine whether they are in the same phase. We use the tensor network representation of Fig. 4, where the interpolating path is characterized by tensors
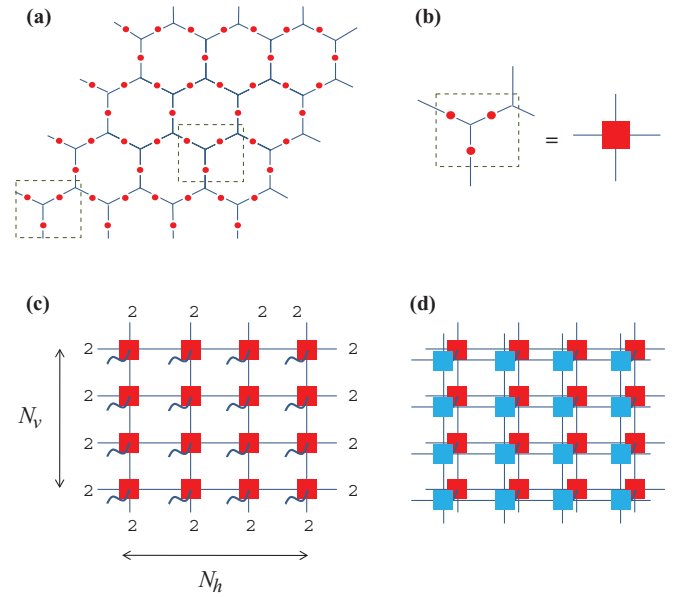

FIG. 10. (Color online) (a) Lattice used for the numerical calculations. The red dots denote $P(\theta)$ tensors. (b) By blocking three spins, we transform this to a square lattice. (c) Resulting square lattice. For OBC, we set the bonds at the boundary to $|2\rangle$ as shown; for CBC, we consider a vertical cylinder where left and right indices are connected. (d) Tensor representation of the scalar product $\langle\Psi(\theta)|\Psi(\theta')\rangle$.

$P(\theta)$ corresponding to $\mathcal{P}(\theta)$ of Eq. (12). For the numerical calculations, it is particularly convenient to block three spins, i.e., $P(\theta)$ tensors, together with two E tensors, as indicated by the dashed squares in Fig. 10(a); this allows us to rewrite the system on a square lattice with three spins per site [Fig. 10(b)]. We perform simulations both for open boundary conditions and for cylindrical boundary conditions. For open boundary conditions (OBC), we set all open indices in the tensor network to $|2\rangle$ (i.e., there are no outgoing singlets at the edges), as indicated in Fig. 10(c). The case of cylindrical boundary conditions is obtained by putting the system on a vertical cylinder, i.e., connecting the left and right indices, while the upper and lower outgoing indices are still set to $|2\rangle$. We will denote by N_h and N_v the number of sites in each row and column of the square lattice, respectively. We will generally consider the case where $N_v \to \infty$ for finite N_h. In this case, cylindrical boundary conditions give the same results as periodic boundary conditions as long as topological degeneracies are appropriately taken into account, and we will therefore refer to them as periodic boundary conditions (PBC) in the following.

1. Correlation functions and gap of the transfer operator

First, we have studied the decay of correlation functions along the dimer-RVB interpolation. Correlation functions can be computed for lattices of arbitrary size using standard methods for the contraction of PEPS.[14] We have computed various correlation functions, all of which show an exponential decay with a slope which changes smoothly with θ, and do not exhibit any sign of a phase transition; as an example, Fig. 11 shows the connected dimer-dimer correlation function between two $z \otimes z$ operators [$z = \mathrm{diag}(1, -1, 1)$], where each
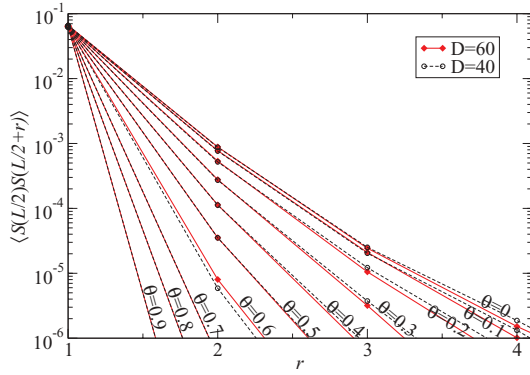
FIG. 11. (Color online) Two-point correlations as a function of the distance for different values of θ. The plot shows data for an infinite system where in the PEPS contraction (Ref. 14) the bond dimension has been truncated at $D = 40$ and $D = 60$, respectively.

dimer is supported on one square tensor of Fig. 10(b) and the two squares are in the same row, as a function of the distance r between the squares, for different values of θ, evaluated on an infinite system. (This data has been obtained by row-wise contraction using infinite matrix product states and iTEBD, and then evaluating the correlation function using the fixed point tensor.)

The decay of any correlation function is bounded by the gap of the transfer operator, i.e., one row in Fig. 10(d). We have used exact diagonalization to determine the gap of the transfer operator for PBC. The result for $N_h = 4, \ldots, 10$, as well as the extrapolated data for $N_h = \infty$, is shown in Fig. 12. Again, the gap of the transfer operator stays finite and converges rapidly for growing N_h. Note that the fact that the ground state is a
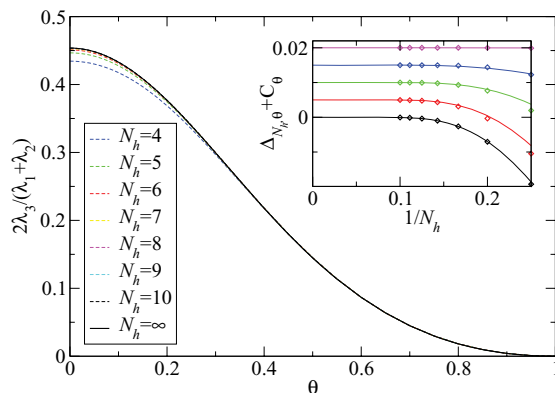

FIG. 12. (Color online) Gap of the transfer operator as a function of θ along the RVB-dimer interpolation for $N_h = 4, \ldots, 10$ and PBC. As the transfer operator is parity preserving (changing) for N_h even (odd), it has two (almost) degenerate largest eigenvalues corresponding to different parity sectors (for N_h even, there is an exponentially small splitting in N_h); the plot shows the ratio of the third eigenvalue and the average of the two maximal eigenvalues. Note that this quantity upper bounds the decay of any correlation function. The data for $N_h = \infty$ has been obtained by fitting the data for $N_h = 6, \ldots, 10$ with $a + b \exp(-cN_h)$. The inset shows the fit for $\theta = 0, 0.1, 0.2, 0.3, 0.5$ (from bottom to top, the curves have been shifted vertically in the plot); note that the two rightmost data points have not been used for the fit.

PEPS throughout the interpolation (and thus satisfies an area law) does not preclude critical behavior.[17,23]

2. Overlap

In order to detect phase transitions which are not reflected in correlation functions, we have also studied the rate at which the state changes as we change θ, as quantified by the overlap (or fidelity).[19] Concretely, let $|\Psi(\theta)\rangle$ be the state interpolating between $|\Psi_{\text{RVB}}\rangle \equiv |\Psi(0)\rangle$ and $|\Psi_{\text{dimer}}\rangle \equiv |\Psi(1)\rangle$, as defined in the preceding section. We define the change of overlap

$$F_{N_h,N_v}(\theta,\epsilon) := \frac{1}{\epsilon^2}\left[1 - \frac{|\langle\Psi(\theta+\epsilon)|\Psi(\theta)\rangle|^2}{\langle\Psi(\theta+\epsilon)|\Psi(\theta+\epsilon)\rangle\langle\Psi(\theta)|\Psi(\theta)\rangle}\right]$$

and are interested in the behavior of the limit

$$f(\theta) = \lim_{N_v, N_h \to \infty} \lim_{\epsilon \to 0} \frac{1}{N_v N_h} F_{N_h,N_v}(\theta,\epsilon) \qquad (13)$$

which describes how quickly the state changes in the thermodynamic limit.

We have computed this quantity in two different ways. In the first approach, we use that for sufficiently small N_h we can exactly compute $F_{N_h,N_v}(\theta,\epsilon)$ for arbitrary values of N_v and ϵ by exact row-wise contraction of the tensor network Fig. 10(d), and use this to extrapolate the limit

$$\hat{F}_{N_h}(\theta) = \lim_{N_v \to \infty} \lim_{\epsilon \to 0} \frac{1}{N_h N_v} F_{N_h,N_v}(\theta,\epsilon) \qquad (14)$$

to arbitrary accuracy for $N_h = 4, 6, 8$; this data is then used in a finite size scaling analysis to infer $f(\theta) \equiv \lim \hat{F}_{N_h}(\theta)$. We apply this approach to the OBC case. The second approach makes use of the fact that $\lim_{\epsilon \to 0} F_{N_h,N_v}(\theta,\epsilon)$ can be expressed as an average over correlation functions, as we show in Appendix B. Again, this average over correlation functions can be computed exactly for any value of N_v, and $N_h \leqslant 10$ [to reach $N = 10$, we use that total bond dimension of the transfer operator of the P tensor, and thus the overall bond dimension in the tensor network in Fig. 10(d), can be reduced from $D^2 = 9$ to 6], which again allows us to determine $\hat{F}_{N_h}$ for $N_h = 4, 6, 8, 10$, and subsequently apply a finite size scaling analysis. We apply this approach to the PBC case.

The resulting data are shown in Fig. 13, together with extrapolated data for $N_h = \infty$ from the finite size scaling. (See Fig. 14 for a discussion of the finite size scaling analysis.) The extrapolated curves for open and periodic boundary conditions agree very well. The extrapolated value for $f(\theta)$ seems to become essentially constant for $\theta \lesssim 0.15$, which might suggest a nonanalytic behavior of $f(\theta)$; however, zooming into this region (inset of Fig. 13) shows clearly that $f(\theta)$ decreases again for $\theta \lesssim 0.12$, showing no evidence for the presence of a phase transition. (See Fig. 14 for a discussion of the difference observed between the extrapolated OBC and PBC data.)

3. Entanglement spectrum

Finally, we have also studied the behavior of the entanglement spectrum along the interpolation for an infinite cylinder, using the techniques described in Refs. 24 and 25 (in particular, using exact contraction). In Fig. 15 we give the entanglement spectra for $N_h = 8$ for the integer and half-integer spin sector (the boundary Hamiltonian does not couple the two sectors).
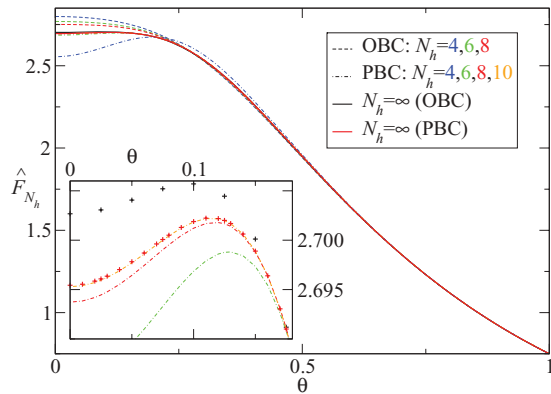
FIG. 13. (Color online) The overlap change $\hat{F}_{N_h}$, Eq. (14), as a function of θ for both open boundary conditions ($N_h = 4,6,8$) and periodic boundary conditions ($N_h = 4,6,8,10$). The solid black and red lines give the extrapolated data for $N_h = \infty$ for open and periodic boundaries. The inset shows a zoom of the $N_h = \infty$ data for $\theta \leqslant 0.18$, where the black (red) crosses correspond to open (periodic) boundaries. The details of the scaling analysis are given in Fig. 14.

While at first, it seems that the lowest lying $S = \frac{1}{2}$ and $S = 1$ states cross with the $S = 0$ ground state at some small θ, a scaling analysis (Fig. 16) suggests that the gap of the entanglement Hamiltonian is more likely to vanish at $\theta = 0$; also, note that there is no prior reason to assume that a vanishing gap in the entanglement spectrum implies any critical behavior in the actual system, as the boundary state is a thermal state of the entanglement Hamiltonian and therefore will have finite correlations even for a critical entanglement Hamiltonian.[25]

Let us also point out an interesting aspect of the entanglement spectrum: While the system under consideration is topological (rigorously provable in an environment of the dimer point[26]), the entanglement Hamiltonian has a
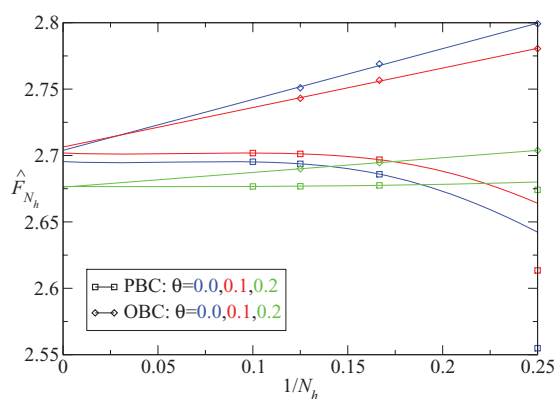

FIG. 14. (Color online) Finite size scaling analysis for $\hat{F}_{N_h}$. The plot shows OBC and PBC data for $\hat{F}_{N_h}$. Due to the absence of boundary effects, the PBC data converge very quickly to the $N_h = \infty$ value once N_h is beyond the correlation length. We have fitted the PBC data for $N_h = 6,8,10$ with $a + b \exp(-cN_h)$. The OBC data, on the other hand, have a $1/N_h$ leading term from the boundary; we have fitted the data for $N_h = 4,6,8$ with $a + b/N_h$. Note that the correction for the data points for OBC would most likely be concave, suggesting that the true $N_h = \infty$ value is closer to the PBC data.

unique ground state, i.e., it is gapped, which shows that the connection between topologically ordered systems and gapless entanglement spectra might be less clear than generally believed. Note that the reason that the entanglement spectrum is gapped (unlike for the toric code, the RK model,[11] or the mapping of Ref. 20) is due to the fact that our representation of the dimer state involves singlets (i.e., an entangled state of two spins) rather than single spins indicating the presence or absence of a dimer, and that we split these singlets when computing the entanglement spectrum, just as one would do for the RVB state itself.

V. HAMILTONIANS

A. Hamiltonian for the dimer state

As has been proven in Ref. 16, every G-injective PEPS on a square lattice appears as the ground state of a local Hamiltonian, acting on at most 2×2 elementary cells, which has a fixed degeneracy determined by the symmetry group. In particular, this result can be directly applied to the dimer state to infer that it is the ground state of a local Hamiltonian with fourfold degeneracy. Alternatively, we can obtain a Hamiltonian for the dimer state by using its local isometric equivalence to the toric code: The same transformation will also transform the toric code Hamiltonian into a local Hamiltonian for the dimer state. Note, however, that we need to add extra terms to the dimer Hamiltonian which ensure that the state is constrained to its local support, as the isometry is only defined as a map between the local support of the toric code and of the dimer state, respectively.

In Appendix C, we explicitly derive a Hamiltonian for the dimer state using the duality with the toric code Hamiltonian. It has three types of terms (all of them projectors), acting on vertices, triangles, and hexagons, respectively:

(1) $h_v^\perp$ acts on individual vertices. It ensures that there is exactly one singlet per vertex.

(2) $h_\triangle^\perp$ acts inside the triangles (as used in the A-B blocking). It makes sure that each triangle holds zero or one singlet.

(3) $h_\bigcirc^\perp$ acts on the six vertices adjacent to each hexagon. It makes sure that all singlet configurations around the corresponding star appear with equal weight.

(The exact form of these three terms, together with their derivation, can be found in Appendix C.)

How does this Hamiltonian compare to the Rokhsar-Kivelson (RK) Hamiltonian for dimer models?[9–11] The resonance terms $h_\bigcirc^\perp$ of our Hamiltonian correspond to those of the RK Hamiltonian; in both cases, they ensure that the ground state is the even weight superposition of all dimer configurations. On the other hand, our Hamiltonian has two additional types of terms ($h_v^\perp$ and $h_\triangle^\perp$) which ensure that the system is in a valid dimer configuration; these terms are not present in the conventional dimer models as they are defined right away on the subspace of valid dimer configurations. While this makes our Hamiltonian more complicated, it is outweighed by the fact that we have a completely local description of our system; in particular, it is this locality of the description which allows us to interpolate between the dimer state and the RVB state locally. Beyond that, the
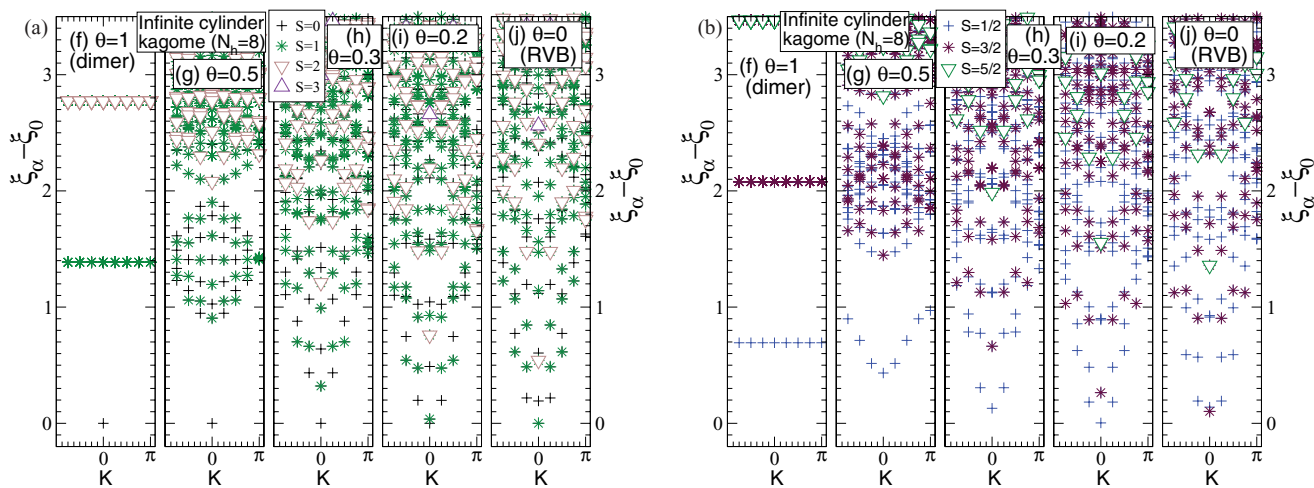
FIG. 15. (Color online) Entanglement spectrum of an infinite (vertical) cylinder for decreasing θ, and perimeter $N_h = 8$. The spectrum is shown as a function of the momentum K along the one-dimensional (horizontal) edge. The eigenstates are also labeled according to their spin quantum numbers ($\frac{1}{2} \oplus 0$ representation) according to the symbols in the legend. Panel (a) shows the integer spin sector of the spectrum, panel (b) the half-integer sector; the two sectors are not coupled by the entanglement Hamiltonian. Note that for both sectors, the same energy scale has been chosen (i.e., trace-normalizing the boundary states in both sectors), corresponding to a local entanglement Hamiltonian (Ref. 24).

particular way in which we make the dimer configurations locally orthogonal allows us to define the resonance moves $h_{\bigcirc}^{\perp}$ on a single hexagon (cf. Appendix C), as compared to the star required in the usual RK Hamiltonian.[11]

B. Hamiltonian for the RVB state

The Hamiltonian $H^{\perp} = \sum h_i^{\perp}$ for the dimer state is *frustration free*; that is, all Hamiltonian terms—which we have chosen to be projectors—annihilate the dimer state, $h_i^{\perp}|\Psi_{\text{dimer}}\rangle = 0$. We can make use of this fact to directly obtain a corresponding frustration-free Hamiltonian for $|\Psi_{\text{RVB}}\rangle = (O_{\bigstar}^{-1})^{\otimes K}|\Psi_{\text{dimer}}\rangle$: Define

$$h_i := \mathcal{O}_{\bigstar}^{\otimes \kappa} h_i^{\perp} \mathcal{O}_{\bigstar}^{\otimes \kappa} \tag{15}$$

where for each i, the product $\mathcal{O}_{\bigstar}^{\otimes \kappa}$ only involves the stars in the covering Fig. 9 which overlap with $h_i^{\perp}$. Then, h_i is positive semidefinite, and $h_i|\Psi_{\text{RVB}}\rangle = 0$. Moreover, for each star k we add a term h_k to the Hamiltonian which

projects onto the orthogonal complement of rg $\mathcal{P}_{\bigstar}$, and thus restricts the ground-state (= zero-energy) subspace of the overall Hamiltonian to rg $\mathcal{P}_{\bigstar}^{\otimes K}$. [Note that conversely, those terms $h_i^{\perp}$ in $H^{\perp}$ which restrict the ground-state space to (rg $\mathcal{P}_{\bigstar}^{\perp})^{\otimes K}$ give $h_i \equiv 0$ in Eq. (15).] As $\mathcal{O}_{\bigstar}^{\otimes K}$ is a bijection between rg $\mathcal{P}_{\bigstar}^{\perp}$ and rg $\mathcal{P}_{\bigstar}$, it follows that there is a one-to-one correspondence between ground states of $H^{\perp}$ and of $H = \sum h_i$; in particular, the constructed RVB parent Hamiltonian has a topology-dependent degeneracy of the ground space (fourfold on the torus), which is obtained from the ground space of the dimer Hamiltonian by applying $\mathcal{O}_{\bigstar}^{\otimes K}$.

The Hamiltonian constructed this way is rather large: In particular, those triangle terms $h_{\triangle}^{\perp}$ which lie at the intersection of three stars give rise to terms acting on three stars in Fig. 9. In order to obtain simpler terms, one can choose to adapt the framework for parent Hamiltonians of G-injective PEPS derived in Ref. 16 to the RVB state, which results in a parent Hamiltonian acting on two overlapping stars, i.e., 19 spins; we give the full derivation in Appendix D.

C. Hamiltonian for the dimer-RVB interpolation

The relation between the dimer and RVB Hamiltonian extends to the whole interpolating path introduced in Sec. IV A, and gives rise to a continuous path of local Hamiltonians interpolating between the dimer model and the RVB state: In order to ensure continuity, we first replace the dimer Hamiltonian $H^{\perp} = \sum_i h_i^{\perp}$ by an equivalent Hamiltonian $\hat{H}^{\perp} := \sum_i \hat{h}_i^{\perp} + \sum_j \Pi_j$. Here, $\hat{h}_i^{\perp}$ is the projection of $h_i^{\perp}$ onto (rg $\mathcal{P}_{\bigstar}^{\perp})^{\kappa(i)}$, where the tensor product $\otimes \kappa(i)$ goes over all stars supporting h_i and we omit vanishing $\hat{h}_i^{\perp}$, and Π_j is the projector onto rg $\mathcal{P}_{\bigstar}^{\perp}$ on star j, where the sum ranges over all stars. As $H^{\perp}$ is a parent Hamiltonian, the restriction to rg $\mathcal{P}_{\bigstar}^{\perp}$ is ensured by the terms in $H^{\perp}$ locally; thus, $\hat{H}^{\perp}$ has the same ground-state space as $H^{\perp}$ with a spectral gap above, and we can
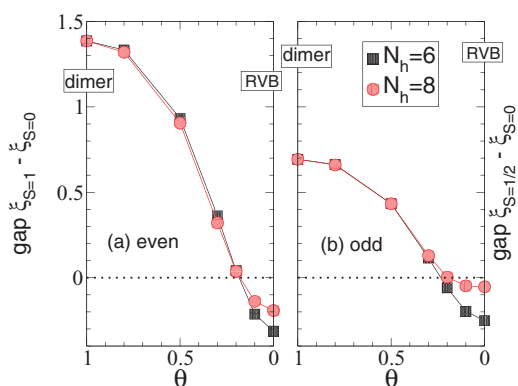

FIG. 16. (Color online) Gap between the lowest $S = 1$ and $S = 0$ state (left) and $S = \frac{1}{2}$ and $S = 0$ state (right) of the entanglement Hamiltonian for the dimer-RVB interpolation for $N_h = 6,8$.

smoothly interpolate between $H^\perp$ and $\hat{H}^\perp$ without changing the ground-state space or closing the gap. For $\hat{H}^\perp$, it is now straightforward to construct a continuous interpolating path $\hat{H}(\theta) = \sum_i \hat{h}_i(\theta) + \Pi_j(\theta)$, where $\hat{h}_i(\theta) = \mathcal{O}_{\bigstar}^{\otimes\kappa}(\theta)\hat{h}_i\mathcal{O}_{\bigstar}^{\otimes\kappa}(\theta)$, and $\Pi_j(\theta)$ projects onto rg $P_{\bigstar}(\theta)$ for star j.

VI. CONCLUSIONS

In this paper, we have applied the PEPS formalism to the study of the resonating valence bond states and dimer models. We have discussed PEPS representations of the RVB and the dimer model and studied their structure and relation. In particular, we have given a local unitary mapping between the dimer model and the toric code; furthermore, by defining the dimer state with locally orthogonal dimers, we were able to devise a local reversible mapping between the dimer state and the RVB state which allowed us to prove that the RVB state is the fourfold degenerate ground state of a local parent Hamiltonian for any finite lattice. Subsequently, this allowed us to devise a smooth interpolation between the dimer state and the RVB state and the corresponding Hamiltonians. We have studied this interpolating path numerically, considering the behavior of correlation functions, the rate at which the ground state changes, and the entanglement spectrum, and have found that all of these quantities behave smoothly and show no sign of a phase transition.

Our results make heavy use of the formalism of PEPS and their associated parent Hamiltonians, and in particular of G injectivity and G isometry, which we generalize in order to assess the RVB state on the kagome lattice. Similarly, the PEPS representation of the dimer-RVB interpolation allowed for efficient numerical simulations, enabling us to study the phase of the RVB state. We believe that these techniques will be of further use in the study of related systems. In particular, the results can be generalized to other lattices: First, the PEPS description of RVB states applies to arbitrary graphs. All lattices with the "linear independence property"[8,27,28] are G injective, and whenever the linearly independent blocks allow cover the lattice up to disconnected patches (such as in Fig. 9); this allows interpolating between the RVB and the corresponding dimer state. (This is the case, for instance, for the square-octagon or the star lattice in Ref. 28, whereas for the hexagonal lattice it appears that no such covering can be found.) Further, if the dimer model can be expressed in terms of $\mathbb{Z}_2$-injective tensors, this allows us to conclude that it is equivalent to the toric code. (This is the case, e.g., for the star lattice, but not for the square-octagon lattice.) Also note that our findings are not restricted to spin-$\frac{1}{2}$ SU(2) singlets as dimers, but can be generalized to higher dimensional singlets or any other state, as long as $\mathbb{Z}_2$ injectivity can be established.

ACKNOWLEDGMENTS

APPENDIX A: DIFFERENT PEPS REPRESENTATIONS FOR THE RVB AND DIMER STATE

In this Appendix, we give an overview of different PEPS representations of the RVB and dimer state and how they are related. We will start from the representation introduced in Ref. 17, and subsequently show how to derive from it the representation used in this paper.

1. PEPS representation of the RVB

We first explain the PEPS representation of the RVB state introduced in Ref. 17, which is illustrated in Fig. 17: We place states

$$|\omega\rangle = |01\rangle - |10\rangle + |22\rangle \in \mathbb{C}^3 \otimes \mathbb{C}^3 \tag{A1}$$

along all edges of the lattice (observing its orientation); this associates four three-level systems (qutrits) with each vertex. Then, we apply the following map to the qutrits at each vertex, which maps them to one physical qubit:

$$
\begin{aligned}
\mathcal{P}_4 = &|0\rangle(\langle 0222| + \langle 2022| + \langle 2202| + \langle 2220|) \\
&+ |1\rangle(\langle 1222| + \langle 2122| + \langle 2212| + \langle 2221|) \\
= &\sum_{k=1}^{4}(|0\rangle\langle 0|_k + |1\rangle\langle 1|_k) \otimes \langle 222|_{/k}. \tag{A2}
\end{aligned}
$$

Here, in the second formulation the sum runs over the four virtual systems k, $\langle 0|_k$ and $\langle 1|_k$ act on the virtual system k, and $\langle 222|_{/k}$ acts on all virtual systems but k.

What is the intuition underlying this construction? The Hilbert space holding the bond state, $|\omega\rangle = |01\rangle - |10\rangle +$
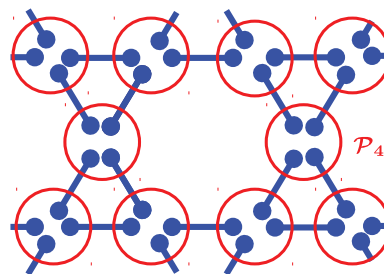

FIG. 17. (Color online) PEPS representation for the RVB. Place maximally entangled "bonds" $|01\rangle - |10\rangle + |22\rangle$ along the edges of the lattice (blue), and subsequently apply the linear map ("PEPS projector") P4 (red circle), Eq. (A2), which maps the four qutrits at each vertex (encircled) to a spin-$\frac{1}{2}$ degree of freedom. Alternatively, we can obtain the (orthogonal) dimer state by replacing $\mathcal{P}_4$ with $\mathcal{P}_{4,\perp}$, Eq. (A3): $\mathcal{P}_{4,\perp}$ ensures that only one qutrit per vertex holds a singlet, but keeps the full Hilbert space, thus ensuring local orthogonality of different dimer configurations.

$|22\rangle$, Eq. (A1), should be understood as a direct sum $\mathbb{C}^2 \oplus \mathbb{C}^1$ [with a corresponding SU(2) representation $\frac{1}{2} \oplus 0$]. The two-dimensional subspace, $\mathfrak{S} = \text{span}\{|0\rangle, |1\rangle\}$, provides the spin-$\frac{1}{2}$ degree of freedom which holds the singlets $|01\rangle - |10\rangle$ used to construct the RVB state, while the third level, $|22\rangle$, is used as a tag indicating that there is no singlet along that edge, synchronizing this choice for both ends. In order to understand what happens when we apply $\mathcal{P}_4$ to the bonds $|\omega\rangle$, let us rewrite $\mathcal{P}_4$ as

$$\mathcal{P}_4 = \mathcal{P}_4 \, \mathcal{P}_{4,\perp},$$

where $\mathcal{P}_{4,\perp}$ is a projector acting *within* the virtual space as

$$\mathcal{P}_{4,\perp} = \sum_{k=1}^{4} \mathbb{1}_{\mathfrak{S},k} \otimes |222\rangle_{/k}\langle 222|_{/k}, \tag{A3}$$

with $\mathbb{1}_{\mathfrak{S},k}$ the projector onto the subspace $\mathfrak{S}$ on site k. Thus, $\mathcal{P}_{4,\perp}$ projects *one* virtual qutrit onto the "singlet space" $\mathfrak{S}$, while the others are projected onto the $|2\rangle$ subspace. Due to the form of $|\omega\rangle$, it follows that both sides of each bond have to be projected onto the same subspace; i.e., either the singlet is selected, or both ends of the bond need to be in the $|2\rangle$ state. From these two observations, it follows that by applying $\mathcal{P}_{4,\perp}$ to the bonds $|\omega\rangle$, we obtain configurations with singlets along the edges, such that exactly one singlet is incident to each vertex, while all other edges are in the "unused" state $|22\rangle$. This way, all possible dimer configurations are orthogonal—we can infer the location of the dimers by measuring whether we are in the $\mathfrak{S}$ subspace or in the $|2\rangle$ state. Moreover, the final state has an equal weight of all dimer configurations, as $|01\rangle - |10\rangle$ and $|22\rangle$ appear with the same relative weight everywhere. Thus, it follows that the state obtained by applying the maps $\mathcal{P}_{4,\perp}$ to the bonds $|\omega\rangle$ is a realization of the (orthogonal) dimer state.

It is now straightforward to see that applying $\mathcal{P}_4$ to this dimer state gives the actual (nonorthogonal) RVB state: $\mathcal{P}_4$ keeps the singlet degree of freedom at every vertex, but it (coherently) erases the information about the edge the singlet is associated with; as the phases between different dimer locations are chosen to be $+1$, we indeed obtain an equal weight superposition of all dimer coverings with singlets, i.e., the RVB state.

2. Simplified PEPS representation

We will now prove that the PEPS representation of the RVB state Eqs. (A1) and (A2) is equivalent to the form introduced in Sec. II B. We start by rewriting $\mathcal{P}_4$, Eq. (A1), as

$$\mathcal{P}_4 = \mathcal{P} \, (\mathcal{Q} \otimes \mathcal{Q}). \tag{A4}$$

Here, $\mathcal{P} : \mathbb{C}^3 \otimes \mathbb{C}^3 \to \mathbb{C}^2$ is defined just as $\mathcal{P}_4$, but acting only on two virtual systems,

$$\mathcal{P} = |0\rangle(\langle 02| + \langle 20|) + |1\rangle(\langle 12| + \langle 21|)$$

[cf. Eq. (2)], and $\mathcal{Q} : \mathbb{C}^3 \otimes \mathbb{C}^3 \to \mathbb{C}^3$ is defined as

$$\mathcal{Q} = |0\rangle(\langle 02| + \langle 20|) + |1\rangle(\langle 12| + \langle 21|) + |2\rangle\langle 22|;$$

it is straightforward to check that (A4) holds. We choose to apply the $\mathcal{Q}$'s as depicted in Fig. 18(a): Then, applying $\mathcal{Q}^{\otimes 3}$
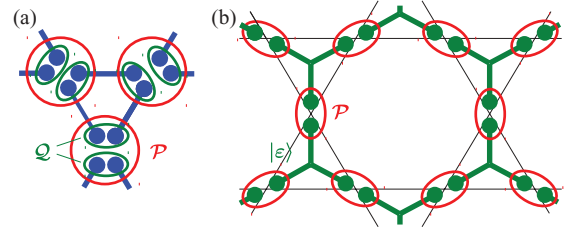

FIG. 18. (Color online) Simplified PEPS construction for the RVB and dimer state. (a) Start from the representation Fig. 17 and rewrite $\mathcal{P}_4$ in two layers, $\mathcal{P}_4 = \mathcal{P}(\mathcal{Q} \otimes \mathcal{Q})$, Eq. (A4). The $\mathcal{Q}$'s act as indicated by the green circles, and make sure *at most* one singlet degree of freedom is kept; they thus return one qutrit each. $\mathcal{P}_2$ makes sure *exactly one* singlet is kept, which can come from either of the two $\mathcal{Q}$'s. (b) The simplified PEPS construction: Applying three $\mathcal{Q}$'s to three bonds around a loop results in a state $|\epsilon\rangle$ which holds at most one singlet, Eq. (A5), and which is placed across every triangle. Subsequently, $\mathcal{P}$ is applied to pick one of the singlets at each vertex.

to $|\omega\rangle^{\otimes 3}$ across each triangle yields a 3-qutrit state

$$|\epsilon\rangle = \sum_{i,j,k=0}^{3} \varepsilon_{ijk}|ijk\rangle + |222\rangle, \tag{A5}$$

where ε_{ijk} is the completely antisymmetric tensor with $\varepsilon_{012} = 1$, where i, j, and k are oriented clockwise. Thus, we obtain a PEPS construction for the RVB state where we place tripartite bond states $|\epsilon\rangle$ across triangles, and apply $\mathcal{P}$ to each adjacent pair of qutrits, as shown in Fig. 18(b).

As already explained in Sec. II C, this PEPS representation of the RVB state can again be understood as arising from a PEPS representation of the dimer state, $\mathcal{P} = \mathcal{P} \, \mathcal{P}_\perp$ with $\mathcal{P}_\perp = \mathbb{1}_{\mathfrak{S}} \otimes |2\rangle\langle 2| + |2\rangle\langle 2| \otimes \mathbb{1}_{\mathfrak{S}}$. Note that different dimer coverings are again locally orthogonal, although in a different fashion—they become orthogonal on triangles. Note that this dimer state can be obtained from the one discussed in the previous section A 1 using that $\mathcal{P}_\perp(\mathcal{Q} \otimes \mathcal{Q}) = (\mathcal{R} \otimes \mathcal{R})\mathcal{P}_{4,\perp}$, where $\mathcal{R} = \mathbb{1}_{\mathfrak{S}} \otimes \langle 2| + \langle 2| \otimes \mathbb{1}_{\mathfrak{S}} + |2\rangle\langle 22|$: While $\mathcal{R}$ removes some degrees of freedom, different dimer configurations remain orthogonal on triangles.

APPENDIX B: CHANGE OF OVERLAP AND CORRELATION FUNCTIONS

In this Appendix, we show how to compute the change of the overlap of the state along the dimer-RVB interpolation from two-point correlation functions; it can be seen as a Hamiltonian-free PEPS version of the result that the change of the overlap can be expressed as an integral over imaginary time correlation functions.[29] While we will illustrate the derivation for the particular case of the dimer-RVB interpolation, it will equally apply to most other PEPS interpolations.

The interpolating path is given by

$$|\psi_\theta\rangle = \mathcal{P}_\theta^{\otimes N}|\Omega\rangle, \tag{B1}$$

with $\mathcal{P}_\theta$ as in Eq. (12), and where $|\Omega\rangle \equiv |\Psi_{\text{dimer}}\rangle$ is the dimer state. $\mathcal{P}_\theta$ can be split as

$$\mathcal{P}_\theta = P_+ + \theta P_-, \tag{B2}$$

where P_+ and P_- are projectors independent of θ, $P_+ + P_- = \mathbb{1}$; the following derivation holds for any interpolation of the form Eqs. (B1) and (B2). Note that from (B2), we have that

$$\mathcal{P}_{\theta+d\theta} = \left(\mathbb{1} + \frac{1}{\theta}P_- d\theta\right)\mathcal{P}_\theta. \tag{B3}$$

We want to compute the change of the normalized overlap

$$O(\theta, \theta + d\theta) = \frac{\langle\psi_\theta|\psi_{\theta+d\theta}\rangle}{\sqrt{\langle\psi_\theta|\psi_\theta\rangle}\sqrt{\langle\psi_{\theta+d\theta}|\psi_{\theta+d\theta}\rangle}}.$$

As the first-order change to $O(\theta, d\theta)$ can be at most a (unphysical) phase change, we are interested in the second order in $d\theta$. We write $|\psi_{\theta+d\theta}\rangle = |\psi_\theta\rangle + |d\psi_\theta\rangle$, and from Eqs. (B1) and (B3), it follows that $|d\psi_\theta\rangle$ can be expanded in orders of $d\theta$.

For notational convenience, let us define

$$\mathcal{N} = \langle\psi_\theta|\psi_\theta\rangle, \quad A = \langle\psi_\theta|d\psi_\theta\rangle/\mathcal{N}, \quad B = \langle d\psi_\theta|d\psi_\theta\rangle/\mathcal{N}.$$

Note that since both $|\Omega\rangle$ and $\mathcal{P}_\theta$ in Eq. (B1) are real, $|\psi_\theta\rangle$ is real, and thus A is real; we will use this in the following derivation. Using the above definitions (where A is first order and B second order in $d\theta$) we have (neglecting third and higher order terms)

$$O(\theta, \theta + d\theta) = \frac{\mathcal{N}(1 + A)}{\mathcal{N}\sqrt{1 + (2A + B)}}$$

$$\approx (1 + A)\left[1 - \frac{2A + B}{2} + \frac{3(2A)^2}{8}\right]$$

$$= 1 - \frac{1}{2}(B - A^2).$$

Clearly,

$$|d\psi_\theta\rangle = \sum \frac{d\mathcal{P}_\theta}{d\theta}\mathcal{P}_\theta^{\otimes(N-1)}|\Omega\rangle d\theta = \sum_i \frac{1}{\theta}P_-^i|\psi_\theta\rangle d\theta,$$

where the sum is over all possible positions i of the $\frac{1}{\theta}P_-^i$. (As A only appears as A^2 in the overlap, we can neglect the second order term.) It follows that

$$A = \frac{1}{\theta}\sum_i \frac{\langle\psi_\theta|P_-^i|\psi_\theta\rangle}{\mathcal{N}} d\theta \equiv \frac{1}{\theta}\sum_i \langle P_-^i\rangle_\theta d\theta,$$

where we have used the notation

$$\langle X\rangle_\theta := \frac{\langle\psi_\theta|X|\psi_\theta\rangle}{\langle\psi_\theta|\psi_\theta\rangle}.$$

On the other hand, to second order

$$B = \frac{1}{\theta^2}\sum_{ij}\langle P_-^i P_-^j\rangle_\theta (d\theta)^2,$$

and thus, the second-order term in the expansion

$$O(\theta, \theta + d\theta) = 1 - \frac{1}{2}g_\theta N(d\theta)^2$$

can be expressed as an average over connected correlation functions:

$$g_\theta = \frac{B - A^2}{N(d\theta)^2} = \frac{1}{\theta^2 N}\sum_{ij}\langle\hat{P}_-^i \hat{P}_-^j\rangle_\theta, \tag{B4}$$

where $\hat{P}_-^i := P_-^i - \langle P_-^i\rangle_\theta$, and N is the number of sites. This derivation shows that for PEPS interpolations, we can infer the change of the overlap from two-point correlators; this argument can be extended to relate the pth order expansion coefficient of the overlap to p-point correlators.

For systems with finite correlation length ξ, the sum in Eq. (B4) is proportional to $\xi^2 N$, and thus, $g_\theta \sim \xi^2/\theta^2$. Therefore, the only way g_θ can diverge when the correlation functions decay exponentially is if $\theta \to 0$. Note, however, that for $\theta = 0$, $\langle\hat{P}_-^i \hat{P}_-^j\rangle_\theta = 0$, so whether g_θ diverges at $\theta \to 0$ depends on the rate at which the latter vanishes.

Note that Eq. (B4) does not apply when $\theta = 0$. For that case, one can easily check that $\langle\psi_{\theta=0}|d\psi_{\theta=0}\rangle = 0$ and thus $A = 0$. On the other hand, $\langle d\psi_{\theta=0}|d\psi_{\theta=0}\rangle/(d\theta)^2$ is the norm of the PEPS where $\mathcal{P}_{\theta=0} \equiv P_+$ has been replaced by P_- at a single site (summed over all sites), which immediately shows how to compute $g_0 = B/N(d\theta)^2$.

APPENDIX C: A SIMPLE PARENT HAMILTONIAN FOR THE ORTHOGONAL RVB

In this Appendix, we show how to directly derive a parent Hamiltonian for the dimer state (in the representation of Sec. II C) by relating it to the toric code on the same lattice. Let us start by considering the toric code model on a kagome lattice, where the spins sit on the edges of the lattice, as illustrated in Fig. 19(a). The toric code Hamiltonian has two types of terms: First, it has terms acting on the four qubits across each vertex, as
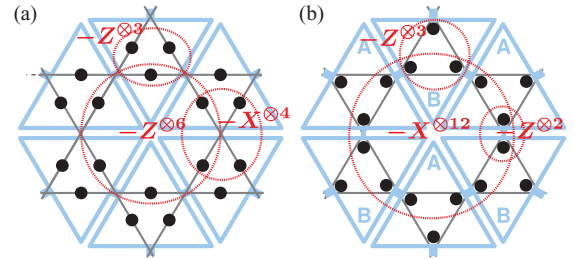
$$h_v^{TC} = -X^{\otimes 4},$$

FIG. 19. (Color online) (a) Tensor network and Hamiltonian for the toric code on the kagome lattice. Two types of terms ensure the parity constraints over the triangular and hexagonal plaquettes, while the vertex term enforces an equal weight superposition of all even parity configurations. Note that the $-Z^{\otimes 3}$ acting on the triangles can be understood as enforcing each individual tensor to be in the correct subspace. (b) Hamiltonian terms obtained by transforming each tensor unitarily into a projector onto the symmetric subspace. $Z^{\otimes 3}$ still enforces that the tensor is in the correct subspace; further, there is a $Z^{\otimes 2}$ at each vertex enforcing equality of the adjacent qubits—translated to the dimer state, this will enforce that there is exactly one singlet adjacent to each vertex. Finally, the $X^{\otimes 12}$ term around the hexagon makes sure that all such configurations appear with equal weight—it will make the dimer configurations resonate in the orthogonal RVB state. (Note that this model can also be understood as a toric code model on a "decorated" hexagonal lattice with two sites per edge and a vertex between, and X stabilizers around plaquettes and Z stabilizers across vertices.)

and second, it has terms acting across plaquettes—triangles and hexagons—as

$$h_\triangle^{TC} = h_\triangledown^{TC} = -Z^{\otimes 3}, \quad h_\bigcirc^{TC} = -Z^{\otimes 6},$$

where X and Z are the Pauli matrices. For future purposes, we have introduced different labels for the two types of triangles: $h_\triangle^{TC}$ refers to an upward pointing *tensor* [sketched blue in Fig. 19(a)], and thus to a downwards triangle, and vice versa. In analogy to the square lattice toric code, Eq. (6), we can write the toric code state with triangular $\mathbb{Z}_2$-invariant tensors

$$\mathcal{P}^{TC} = \sum_{\alpha,\beta,\gamma} = |\alpha - \beta, \beta - \gamma, \gamma - \alpha\rangle\langle\hat{\alpha}, \hat{\beta}, \hat{\gamma}|.$$

The states $\langle\hat{\eta}|$ on the virtual level are again in the x eigenbasis, which makes them invariant under $Z^{\otimes 3}$. The tensors are marked blue in Fig. 19(a), with the virtual indices associated with vertices of the kagome lattice. $\mathcal{P}^{TC}$ can be transformed by a unitary acting on the physical system to the projector onto the invariant subspace,

$$\tilde{\mathcal{P}}^{TC} = \tfrac{1}{2}(\mathbb{1}^{\otimes 3} + Z^{\otimes 3}),$$

where the physical qubits are now associated with vertices; cf. Fig. 19(b). It can be easily checked that the action of the Hamiltonian terms in the transformed basis is as follows [illustrated in Fig. 19(b)]:

$$\tilde{h}_v^{TC} = -Z^{\otimes 2}$$

enforces that the two qubits per vertex are in the same state (namely equal to the value of the virtual index);

$$\tilde{h}_\bigcirc^{TC} = -X^{\otimes 12}$$

acts on the 12 qubits around each hexagon and ensures that all bond configuration appear with the same probability; finally, in the original representation, $h_\triangle^{TC} = h_\triangle^{TC}$ enforced that the qubits at each tensor are in the proper subspace; it thus has to be replaced by the corresponding term for the transformed tensor,

$$\tilde{h}_\triangle^{TC} = \tilde{h}_\triangledown^{TC} = -Z^{\otimes 3}.$$

The three terms are depicted in Fig. 19(b).

Let us now consider what happens if we change all A-type tensors (upwards pointing triangles) to projectors onto the antisymmetric subspace,

$$\tilde{\mathcal{P}}_\triangle^{def} = \tfrac{1}{2}(\mathbb{1}^{\otimes 3} - Z^{\otimes 3}),$$

while the B-type tensors (downwards pointing triangles) remain of the form

$$\tilde{\mathcal{P}}_\triangledown^{def} = \tfrac{1}{2}(\mathbb{1}^{\otimes 3} + Z^{\otimes 3}).$$

Clearly, this gives rise to a different triangular Hamiltonian for all A-type tensors,

$$\tilde{h}_\triangle^{def} = Z^{\otimes 3},$$

which enforces odd parity, while we keep $\tilde{h}_\triangledown^{def} = \tilde{h}_\triangledown^{TC}$ for the B-type tensors. All other Hamiltonian terms remain unchanged, since we still need to ensure that the qubits on both sides of the vertex are equal ($\tilde{h}_v^{def} = \tilde{h}_v^{TC}$), and that all configurations appear in an equal weight superposition ($\tilde{h}_\bigcirc^{def} = \tilde{h}_\bigcirc^{TC}$).

The projectors $\tilde{\mathcal{P}}_\triangle^{def}$ and $\tilde{\mathcal{P}}_\triangledown^{def}$ can now be transformed to the A and B tensors for the dimer state by local isometries, which

allows us to explicitly construct its parent Hamiltonian: First, the terms $\tilde{h}_\triangle^{def}$ and $\tilde{h}_\triangledown^{def}$ enforce that the sites at each tensor are in the correct subspace; they are thus mapped to a local term $h_\triangledown = h_\triangle$ which have the four states of Fig. 7 as ground states. The vertex term $\tilde{h}_v^{def}$ is transformed to

$$h_v = -(\mathbb{1}_\mathfrak{S} \otimes |2\rangle\langle 2| + |2\rangle\langle 2| \otimes \mathbb{1}_\mathfrak{S}),$$

$\mathfrak{S} = \text{span}\{|0\rangle, |1\rangle\}$, which ensures there is only one singlet adjacent to each vertex. Finally, $\tilde{h}_\bigcirc^{def}$ is transformed to a term which swaps the singlet/no-singlet configuration for the 12 qutrits adjacent to each hexagon, observing the orientation of the singlets: This is achieved by an operator

$$h_\bigcirc = -\Xi^{\otimes 6},$$

where Ξ acts on the two qutrits in each triangle adjacent to the hexagon as

$$\Xi = |22\rangle(\langle 01| - \langle 10|) - |20\rangle\langle 02| - |21\rangle\langle 12| + \text{H.c.},\tag{C1}$$

with proper orientation of the singlet—the first term changes between a singlet and no singlet along the edge, and the latter two terms flip the location of a (outwards-pointing) singlet in the triangle; the negative sign is due to the fact that the two singlets are oriented differently. The action of Ξ is illustrated in Fig. 20(a). Note that this $\Xi^{\otimes 6}$, although it acts on a hexagon only, in fact achieves resonance between all loop configurations on the star built around the hexagon, as illustrated in Fig. 20(b) for a particular instance.

APPENDIX D: *G*-INJECTIVE TOOLBOX AND PARENT HAMILTONIAN FOR THE RVB STATE

In the main text, we have seen how to manipulate the RVB state in a kagome lattice, to connect it with the dimer state and then with the toric code in such a way that we can apply the results about $\mathbb{Z}_2$-injective PEPS given in Ref. 16 to give a local frustration-free Hamiltonian with topological features for the RVB state. Another possible approach is to modify the toolbox for *G*-injective PEPS developed in Ref. 16 to adapt it to lattices different than the square one, even frustrated ones.
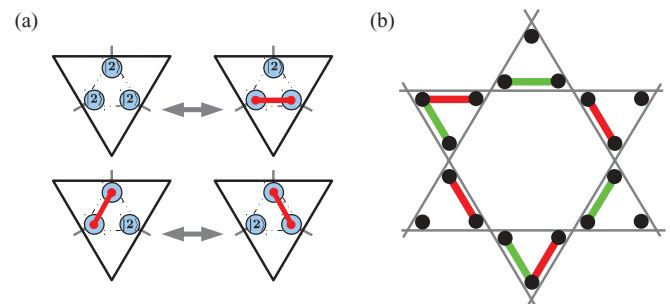

FIG. 20. (Color online) Resonance moves in the dimer state. (a) Resonance move implemented by a single Ξ, Eq. (C1): Ξ acts on the lower two qutrits only and flips the two configurations singlet/no singlet, and the two configurations singlet left/singlet right. (b) Applying $\Xi^{\otimes 6}$ around the hexagon gives a resonance between pairs of dimer configurations around the hexagon (marked red and green, respectively). Note that any such pair of dimer configuration can be described by a closed loop of even length on the star; cf. Ref. 8.

Since this route is necessarily technical, and assumes the reader is familiar with Ref. 16, we only sketch it in this appendix. The payoff: a more local Hamiltonian—acting on two partially overlapping stars, that is, 19 spins—and the possibility of applying the G-injectivity toolbox to rather general lattices in the future.

For simplicity, we will stick to $\mathbb{Z}_2$ injectivity and the kagome lattice, but it is straightforward how to extend the ideas to general finite groups and general lattices. We will work with the tensor network picture of the RVB state given in Fig. 4(b), where the RVB state is recovered from contracting two types of tensors P and E. In the first part of this appendix, Secs. D1 to D3, we will generalize the three key ingredients of Ref. 16: (i) showing that $\mathbb{Z}_2$ injectivity is stable while growing the lattice, (ii) showing the "intersection property" for good-shaped Hamiltonians—as the one acting on three overlapping stars—and (iii) showing that we recover the desired ground space while closing the boundaries. All that will produce a local frustration-free Hamiltonian for the RVB state with local terms acting on three overlapping stars and 4-fold degeneracy. Finally, in Sec. D4, we will see how to reduce the size of the local Hamiltonian to two overlapping stars. For that, we will need the concept of linear independence introduced by Seidel in Ref. 8.

1. Growing $\mathbb{Z}_2$ injectivity

We recall from the main text that a region in a tensor network is $\mathbb{Z}_2$ injective if it is $\mathbb{Z}_2$ invariant, as illustrated in Fig. 5, and in addition one can left-invert the tensor in that region (understood as a map from the auxiliary to the physical system) to get the projection onto the invariant subspace. In Fig. 8 of the main text, the basic $\mathbb{Z}_2$-injective block—one star—is depicted. In Fig. 21 we illustrate how to grow the $\mathbb{Z}_2$-injective property from one to two partially overlapping stars, but the procedure can be applied to grow arbitrarily large regions. The only basic property we need for that is the possibility of decomposing the final tensor as in Fig. 21(a), and that this property is preserved as we grow the region. The general result is that for regions that are grown keeping this property (it is trivial that one can grow in this way all regions that are required to be $\mathbb{Z}_2$ injective later on in this appendix), there is an inverse giving the projector onto the invariant subspace:

$$\frac{1}{2}\sum_{r=0}^{1}(-1)^{|t|r}\bar{Z}^{r\,\otimes|b|},$$

where $|t|$ is the number of tensors, both of P and E type, $|b|$ is the number of outgoing indices in the region, and

$$\bar{Z} := \begin{pmatrix} 1 & & \\ & 1 & \\ & & -1 \end{pmatrix}.$$

As commented in the main text, the extra sign one obtains depending on the parity of the number of elementary tensors in the region only affects the definition of "invariant subspace," which can be the symmetric ($|t|$ even) or the antisymmetric one ($|t|$ odd).
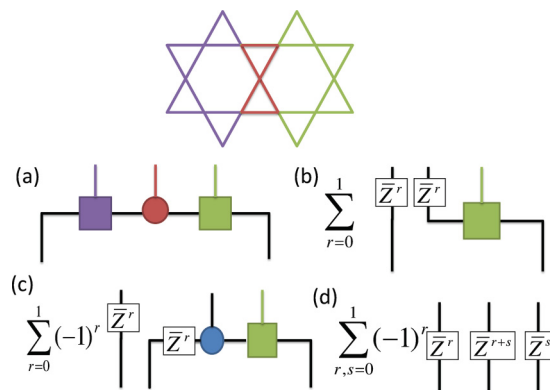

FIG. 21. (Color online) Graphical proof that $\mathbb{Z}_2$ injectivity is stable as growing a region. We illustrate it in the case of growing from one to two partially overlapping stars. Our aim is to prove the existence of a left inverse on the invariant subspace on the two stars, using the existence of the left inverse on a single star. Since we are considering the tensor network representation of the RVB state made out of tensors P—with physical index—and triangular links E without physical index, given a region, all one needs is to clarify whether the outgoing auxiliary indices come from a P tensor or from an E tensor. In our case, we start with two overlapping stars with outgoing indices of type P and divide them into three regions, the middle one (bow tie) with all outgoing indices of type P and the rest. By gathering indices together, we have panel (a), where the circle represents the bow tie and each square one of the other two regions. The crucial property is that the circle together with *any* of the two squares is $\mathbb{Z}_2$ injective. We proceed as follows. We apply the inverse to the circle and left square, getting panel (b), where $\bar{Z}$ now means $\otimes\bar{Z}$. The next step, illustrated in (c), is to build a new circle tensor attached to the right square tensor, and passing the $\bar{Z}^r$ through using the symmetry of the circle tensor. Now we invert the remaining two tensors, getting (d). By tracing the middle (extra) line we obtain δ_{rs} and therefore finish the argument since we have constructed the desired inverse.

2. Intersection property

We recall from the main text and Ref. 16 that given a PEPS, one can construct parent Hamiltonians $H = \sum_R h_R$ where the local term h_R only acts on a region R. The way to construct them is simple. Each h_R is the orthogonal projector (or any positive semidefinite operator) whose kernel coincides with the range of the PEPS tensor on that region (seen as a map from the auxiliary to the physical indices in the region). This Hamiltonian is $\geqslant 0$, frustration free, and has the initial PEPS as ground state. In Ref. 16 we noticed how in the square lattice, G injectivity preserves the structure of the parent Hamiltonian as we grow it properly (i.e., by translational invariance) from a single local operator. That is, the kernel of $\sum_{R\subset\mathcal{R}} h_R$ is *exactly* the range of the PEPS tensor in the larger region $\mathcal{R}$. This property is known as the "intersection property" since it is related to the way the kernels of h_R for different regions intersect. We will illustrate here the intersection property for the case $h_1 + h_2$ where h_1 acts on the 3 stars colored in blue-red in Fig. 22(a) and h_2 acts on those colored in red-green. The only property one needs to make the argument work is that the common interaction area is $\mathbb{Z}_2$ injective and that the noncommon areas are not directly connected. The proof is graphically given in Fig. 22.
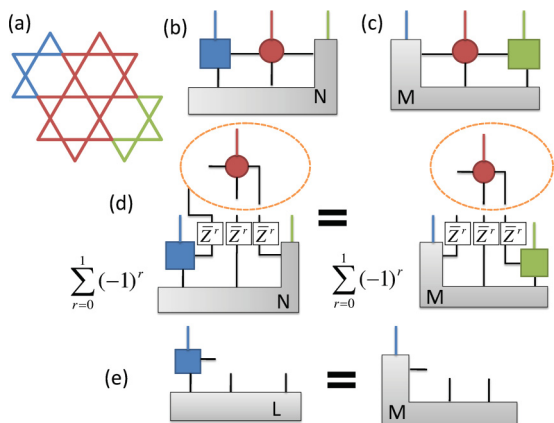
FIG. 22. (Color online) Graphical proof of the intersection property for the case $h_1 + h_2$ where h_1 acts on the 3 stars colored in blue-red in (a) and h_2 acts on those colored in red-green. It is easy to see that by separating the common part (2 red stars) and the rest, with the convention that the common part has all outgoing indices of type P, $\ker h_1 \otimes \mathcal{H}_{\text{green}}$ is given by panel (b), where N is an arbitrary tensor, whereas $\mathcal{H}_{\text{blue}} \otimes \ker h_2$ is given by panel (c), where M is arbitrary. Here $\mathcal{H}_{\text{green}}$ and $\mathcal{H}_{\text{blue}}$ represent the Hilbert spaces associated with the physical indices in the green and blue regions, respectively. As before, we have gathered together all virtual (as well as the physical) indices within each type of tensor. Given a state $|\psi\rangle$ in the intersection of both kernels, there exist N and M such that $|\psi\rangle$ can be expressed both in the form (b) and (c). In the equality (b)=(c) we invert the circle tensor, obtaining the equality given in panel (d). After that, we apply an auxiliary extra circle tensor, then the inverse of the red-green tensors (3 stars), which is also $\mathbb{Z}_2$ injective by the previous section, and then trace the extra virtual system. Since one can assume without loss of generality that both M and N have the symmetry $\otimes \bar{Z}$, we can also eliminate the sums. After all that we arrive at panel (e) for some tensor L. Substituting (e) in (c) gives the desired form for $|\psi\rangle$ and hence the result.

3. Closing the boundaries

It is not difficult to see that if one considers the RVB state as a PEPS in a torus of arbitrary size, by blocking tensors and gathering indices together, one has the tensor network given in Fig. 23(b). It may seem at first sight that we are back to a square-lattice PEPS. However, there is a crucial difference. Not all tensors in the square decomposition of Fig. 23(b) are $\mathbb{Z}_2$ injective. We do require that the four overlapping regions $\mathcal{R}_1, \ldots, \mathcal{R}_4$ resulting from removing one row and one column with an intersecting blue tensor contain all possible 3-star regions and that they can be constructed by growing 3-star regions keeping the intersection property commented on last section. Figure 23(a) illustrates a possible way of getting that in the surrounding of a blue tensor. We will now use the trivial fact that, given the frustration-free Hamiltonian

$$H = \sum_{s \in \{3-\text{star}\}} h_s \qquad (D1)$$

resulting from summing the local projectors corresponding to each 3-star region in the torus, its ground space coincides with $\cap_{k=1}^{4} \ker H_k$, where $H_k = \sum_{s \subset \mathcal{R}_k} h_s$ is the Hamiltonian corresponding to the region $\mathcal{R}_k$. By the intersection property proved in last section, the associated kernels are given by Fig. 24.
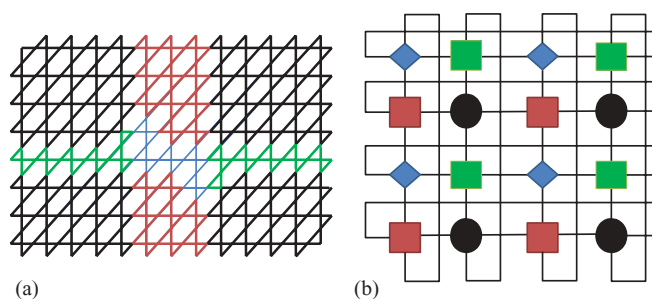

FIG. 23. (Color online) The kagome lattice with periodic boundary conditions can be decomposed as in (b), where all outgoing indices on the black regions are of type P, whereas all outgoing indices of the blue regions are of type E. All tensors in (b) have an additional physical index "going out of the paper." A possible way to obtain such a decomposition is illustrated in (a). The black regions are $\mathbb{Z}_2$ injective; the same happens if one takes two black regions with the intermediate red or green one or if one takes the four black regions with the intermediate red, green, and blue ones. The blue region is the one corresponding to the cross points. Note that the black and the blue only interact through a red or green region, exactly as required in (b).

The argument now is a modification of Theorem 5.5 of Ref. 16. We include a sketch for the sake of completeness. The aim is to show that the ground space of (D1) is spanned by the four states $|\psi_{r,s}\rangle$, $r,s = 0,1$, depicted in Fig. 25.

Using the two horizontal equalities of Fig. 24 and reasoning as in the previous sections (inverting the two columns which are $\mathbb{Z}_2$ injective, growing new tensors around the remaining column, inverting them and taking traces), we obtain that the state is of the form of Fig. 26(a) (from the upper equality in Fig. 24), as well as of the form of Fig. 26(b) (from the lower equality). The vertical equalities then give that Fig. 26(a) equals Fig. 26(b).
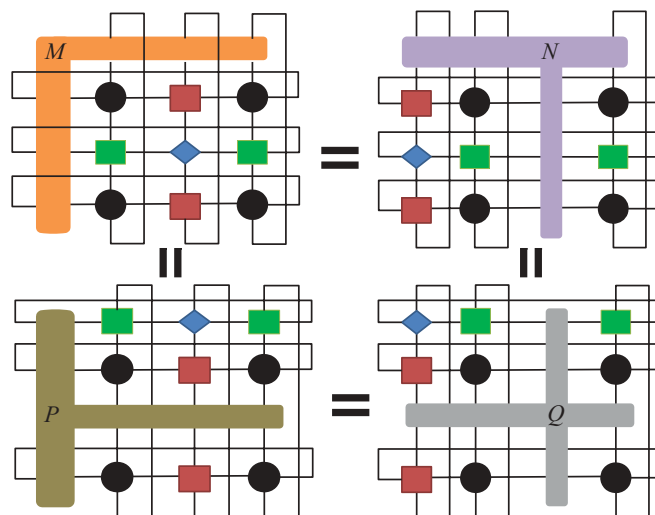

FIG. 24. (Color online) Any state which is in the ground state of the parent Hamiltonian when we close the boundaries in a periodic way [where we close the boundaries as indicated in Fig. 23(a)] can be represented graphically in any of the forms given in the figure. As in Fig. 23, each of the tensors, including the "boundary conditions," have a physical index going "out of the paper."
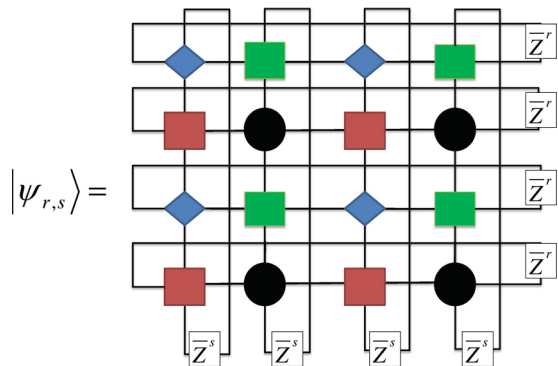
FIG. 25. (Color online) The ground space of the Hamiltonian with periodic boundary conditions has dimension four and is spanned by the states $|\psi_{r,s}\rangle$ in the figure. As above, $\bar{Z}$ means $\otimes\bar{Z}$.

We can now invert the two rows containing black tensors. The way to do it is to invert the two black tensors with one intermediate red one, then construct two new black tensors around the remaining red one, invert again, and take traces. This even allows us to select a particular $r = r_0$, this way removing the sum over r. We end up in Fig. 26(c) and from there, with similar techniques we show that the given state must be a linear combination of states of the form given in Fig. 25. Since clearly all such states belong to the ground space of the Hamiltonian, and all of them are linearly independent, they form a basis of the ground space. Note that as in the toric code, all four ground states are related by nonlocal string operators on the virtual level. Indeed, the action of these virtual operators is nothing but changing the sign (or flipping the direction) of the dimers crossing the links in which they lie. Note also that the same procedure and conclusions can be obtained starting from the parent Hamiltonian of a basic region different from the 3-star one, as long as one can grow properly the lattice starting from this region while keeping the intersection property. Another example of such a basic region is the 7-star region of Fig. 27(a).
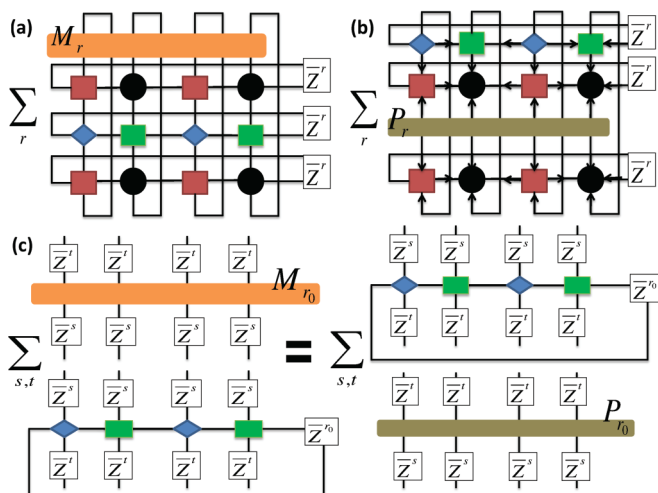

FIG. 26. (Color online) Intermediate step in the proof that the ground space of the Hamiltonian is spanned by the vectors given in Fig. 25 above.
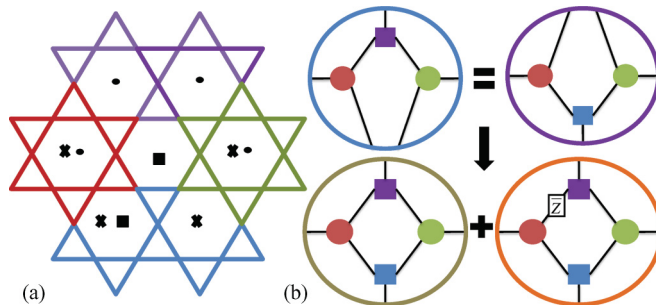

FIG. 27. (Color online) The figure illustrates the first step in the reduction to show that the parent Hamiltonian on two overlapping stars suffices to give the RVB state as a unique ground state—up to the string operators given in Fig. 25 which induce a 4-fold degeneracy. The left (right) upper part of (b) represents the kernel of the Hamiltonian grown from 2-star regions which acts on the stars with a dot (cross). The circles represent the stars with the same color in (a), with all outgoing indices of type P. The squares represent the rest of (a), having outgoing indices both of type P (those connecting with the boundary) and type E (those connecting with the circles). As in the previous figures, all bonds connecting the same objects have been gathered together in the same bond. Also, all tensors have an additional physical index which "goes out of the paper." The boundary conditions in the upper part of (b) have also a physical index corresponding to the part of (a) with the same color. The intersection of these two kernels, which is the kernel of $H_6 = \sum_{x,\circ} H_2$, is the sum of the two subspaces depicted in the lower part of (b). Needless to say that the boundaries of the lower part of (b) do not have physical index.

4. A 2-star Hamiltonian

The first step to show that a 2-star Hamiltonian suffices is sketched in Fig. 27. Starting from the parent Hamiltonian for 2-star regions, and using the intersection property, one gets that the Hamiltonian acting on the four stars marked with a dot (cross) has a kernel equal to the upper-left (upper-right) subspace in Fig. 27(b). Therefore, the kernel of the Hamiltonian $H_6 = \sum_{x,\circ} H_2$—the sum of all terms acting on two overlapping stars marked by both circles or crosses—is the intersection of those subspaces. Take a vector in the intersection. Then we can reason with the very same techniques as above. First we invert the circles, then grow again circles at both sides of the blue square and invert the joint tensor circle-square-circle. Closing the unnecessary indices by taking traces we arrive at the fact that the original tensor indeed belongs to the sum of the subspaces in the lower part of Fig. 27(b). Since clearly each one of these subspaces is contained in the kernel of H_6, the lower part of Fig. 27 is indeed equal to the kernel of H_6.

The second step is to add a 2-star term including the middle star, for instance, the one marked by squares in Fig. 27(a). We will show that this term penalizes all the states in the lower-right subspace of Fig. 27(b). That is, $\cap_{x,\circ,\square} \ker H_2 = \ker\{\sum_{x,\circ,\square} H_2\}$ equals the lower-left subspace in Fig. 27(b), where the intersection/sum runs on all 2-star Hamiltonians in the 7-star region given in Fig. 27(a). This procedure illustrates how from 2-star Hamiltonians one reaches the desired ground space in the 7-star region of Fig. 27(a). Since this ground space is the same one obtains growing from 3-stars, we are done.
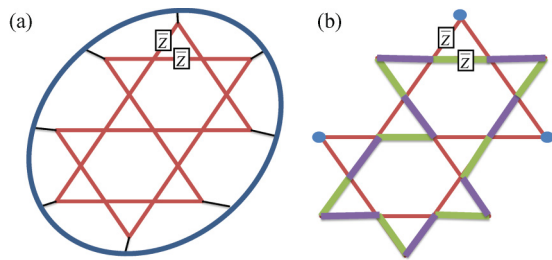
FIG. 28. (Color online) The figure illustrates the second step in the reduction to a 2-star Hamiltonian. (a) represents the space $\mathcal{S}$, coming from the lower-right part of Fig. 27(b), each state of which we want to penalize by the 2-star term marked by squares in Fig. 27(a). All outgoing indices are of type P. (b) illustrates the idea of "completing the path": for each set of free sites—marked by a circle—there exist 2 disjoint dimer coverings (in green and violet, respectively) compatible with the choice of free sites, which in addition form a Hamiltonian cycle in the remaining graph.

Let us first explain the intuition behind the following reasoning. For this, we will use the PEPS representation of the RVB of Fig. 17. The intuition is that the $\bar{Z}$ appearing in the lower-right part of Fig. 27(b)—which denotes nothing but a $\bar{Z}^{\otimes 4}$ in the 4 bonds connecting the corresponding regions—cannot escape the middle star: That is, no matter how we use the gauge symmetry of the tensors in the PEPS, there will be one, and only one, $\bar{Z}$ in one of the bonds of the middle hexagon. This "excitation" can be then detected by a 2-star term including the middle star. To make it rigorous we will need the linear-independence property, proven by

Seidel in Ref. 8: The sum $\oplus_D\{|\sigma(D)\rangle \otimes \mathcal{H}_{D,\text{free}}\}$ is direct. Here, D means a fixed dimer covering of the 2-stars, $|\sigma(D)\rangle$ the associated tensor product of singlets, and $\mathcal{H}_{D,\text{free}}$ the total Hilbert space of those *free* sites which do not have any dimer. The sum runs on all possible dimer coverings of the 2-stars.

Let us now take the Hamiltonian acting on the stars marked with a square in Fig. 27(a). Using the $\mathbb{Z}_2$ injectivity, its kernel is exactly given by $\mathcal{K} = \oplus_b\{\mathcal{H}_b \otimes \sum_{\text{valid}} |\sigma(D)\rangle\}$, where b is a fixed choice of free sites—with an odd number of terms to allow dimer coverings—and the sum runs over all possible dimer coverings having b as the set of free sites. We are then finished if we can show that the subspace $\mathcal{S}$ given by Fig. 28(a) has trivial intersection with $\mathcal{K}$, or equivalently, that the sum $\mathcal{S} \oplus \mathcal{K}$ is direct. By the very definition of the PEPS tensor, $\mathcal{S}$ is given exactly by $\mathcal{S} = \oplus_b\{\mathcal{H}_b \otimes \sum_{\text{valid}} \hat{Z}|\sigma(D)\rangle\}$ where $\hat{Z}$ changes the sign of $|\sigma(D)\rangle$ when D has one dimer on a link marked by $\bar{Z}$ in Fig. 28(a) and only in this case. By the linear independence property of Seidel, the sum $\mathcal{S} \oplus \mathcal{H}$ will be direct as long as we can guarantee that for each b, in $\sum_{\text{valid}} \hat{Z}|\sigma(D)\rangle$ there will be terms in the sum with dimers on the $\bar{Z}$ links and terms without dimers on the $\bar{Z}$ links. This last statement can be easily checked by "completing the path," as illustrated in Fig. 28(b). The fact that for each b, there exists a Hamiltonian cycle of alternating colors for the sites not in b can be easily seen as follows. We can have paths of alternating colors in the desired vertices in all but the middle bow tie. Since b contains an odd number of sites, at one side of the bow tie we arrive with the same color whereas at the other side we arrive with different colors. Exactly as in Fig. 28(b) we can complete the cycle within the bow tie.

[1] P. W. Anderson, Mater. Res. Bull. **8**, 153 (1973).

[2] G. Misguich and C. Lhuillier, in *Frustrated Spin Systems*, edited by H. T. Diep (World-Scientific, 2003).

[3] P. Mendels, F. Bert, M. A. de Vries, A. Olariu, A. Harrison, F. Duc, J. C. Trombe, J. Lord, A. Amato, and C. Baines, Phys. Rev. Lett. **98**, 077204 (2007).

[4] Z. Y. Meng, T. C. Lang, S. Wessel, F. F. Assaad, and A. Muramatsu, Nature (London) **464**, 847 (2010).

[5] F. Mezzacapo and M. Boninsegni, Phys. Rev. B **85**, 060402 (2012).

[6] S. Yan, D. A. Huse, and S. R. White, Science **332**, 1173 (2011).

[7] S. Depenbrock, I. P. McCulloch, and U. Schollwöck, Phys. Rev. Lett. **109**, 067201 (2012).

[8] A. Seidel, Phys. Rev. B **80**, 165131 (2009).

[9] D. S. Rokhsar and S. A. Kivelson, Phys. Rev. Lett. **61**, 2376 (1988).

[10] R. Moessner and S. L. Sondhi, Phys. Rev. Lett. **86**, 1881 (2001).

[11] G. Misguich, D. Serban, and V. Pasquier, Phys. Rev. Lett. **89**, 137202 (2002).

[12] J. Cano and P. Fendley, Phys. Rev. Lett. **105**, 067205 (2010).

[13] F. Verstraete and J. I. Cirac, Phys. Rev. A **70**, 060302 (2004).

[14] F. Verstraete and J. I. Cirac, arXiv:cond-mat/0407066.

[15] D. Perez-Garcia, F. Verstraete, J. I. Cirac, and M. M. Wolf, Quantum Inf. Comput. **8**, 0650 (2008).

[16] N. Schuch, I. Cirac, and D. Pérez-García, Ann. Phys. **325**, 2153 (2010).

[17] F. Verstraete, M. M. Wolf, D. Perez-Garcia, and J. I. Cirac, Phys. Rev. Lett. **96**, 220601 (2006).

[18] A. Kitaev, Ann. Phys. **303**, 2 (2003).

[19] P. Zanardi and N. Paunković, Phys. Rev. E **74**, 031123 (2006).

[20] C. Nayak and K. Shtengel, Phys. Rev. B **64**, 064422 (2001).

[21] V. Elser and C. Zeng, Phys. Rev. B **48**, 13647 (1993).

[22] K. S. Raman, R. Moessner, and S. L. Sondhi, Phys. Rev. B **72**, 064413 (2005).

[23] T. Barthel, M. Kliesch, and J. Eisert, Phys. Rev. Lett. **105**, 010502 (2010).

[24] D. Poilblanc, N. Schuch, D. Pérez-García, and J. I. Cirac, Phys. Rev. B **86**, 014404 (2012).

[25] J. I. Cirac, D. Poilblanc, N. Schuch, and F. Verstraete, Phys. Rev. B **83**, 245134 (2011).

[26] S. Bravyi, M. Hastings, and S. Michalakis, J. Math. Phys. **51**, 093512 (2010).

[27] J. T. Chayes, L. Chayes, and S. A. Kivelson, Commun. Math. Phys. **123**, 53 (1989).

[28] J. Wildeboer and A. Seidel, Phys. Rev. B **83**, 184430 (2011).

[29] L. Campos Venuti and P. Zanardi, Phys. Rev. Lett. **99**, 095701 (2007).